Novel magnetic silk fibroin scaffolds with delayed degradation for potential long-distance vascular repair

Xin Liu [a,1], Yuxiang Sun [a,1], Bo Chen [b], Yan Li [a,**], Peng Zhu [c], Peng Wang [a], Sen Yan [a], Yao Li [d], Fang Yang [a,***], Ning Gu [a,*]

[a] State Key Laboratory of Bioelectronics, Jiangsu Key Laboratory for Biomaterials and Devices, School of Biological Science & Medical Engineering, Southeast University, Nanjing, 210096, PR China
[b] Materials Science and Devices Institute, Suzhou University of Science and Technology, 1 Kerui Road, Suzhou, 215009, PR China
[c] State Key Laboratory of Quality Research in Chinese Medicines, Macau Institute for Applied Research in Medicine and Health, Macau University of Science and Technology, Macau, 999078, PR China
[d] College of Social Sciences, University of Glasgow, Glasgow, G12 8QQ, United Kingdom

ARTICLE INFO

ABSTRACT

Although with the good biological properties, silk fibroin (SF) is immensely restrained in long-distance vascular defect repair due to its relatively fast degradation and inferior mechanical properties. It is necessary to construct a multifunctional composite scaffold based on SF. In this study, a novel magnetic SF scaffold (MSFCs) was prepared by an improved infiltration method. Compared with SF scaffold (SFC), MSFCs were found to have better crystallinity, magnetocaloric properties, and mechanical strength, which was ascribed to the rational introduction of iron-based magnetic nanoparticles (MNPs). Moreover, *in vivo* and *in vitro* experiments demonstrated that the degradation of MSFCs was significantly extended. The mechanism of delayed degradation was correlated with the dual effect that was the newly formed hydrogen bonds between SFC and MNPs and the complexing to tyrosine (Try) to inhibit hydrolase by internal iron atoms. Besides, the β-crystallization of protein in MSFCs was increased with the rise of iron concentration, proving the beneficial effect after MNPS doped. Furthermore, although macrophages could phagocytose the released MNPs, it did not affect their function, and even a reasonable level might cause some cytokines to be upregulated. Finally, *in vitro* and *in vivo* studies demonstrated that MSFCs showed excellent biocompatibility and the growth promotion effect on CD34-labeled vascular endothelial cells (VECs). In conclusion, we confirm that the doping of MNPs can significantly reduce the degradation of SFC and thus provide an innovative perspective of multifunctional biocomposites for tissue engineering.

1. Introduction

Treatment for long-distance (≥10 mm) vascular injury (LDVJ) is a challenge in clinical surgery due to the complexity of the vascular network and the pathological fibrosis caused by the long repair period [1–5]. Currently, vascular scaffold is one of the effective therapies for LDJV [6,7], which can promote the formation of vascular endothelium and the deposition of extracellular matrix [8–10]. The common vascular scaffold materials include synthetic polymer materials and natural

materials [11–13]. Synthetic polymers have been successfully applied to vascular scaffolds for a long time, such as Nylon, Dacron, and Polyurethane [14,15]. Meanwhile, natural materials gradually attracted the attention due to their excellent low immunogenicity and controllable degradation. Unfortunately, natural materials usually have the problems of poor mechanical strength and mismatched degradability for different damaged tissues [4,16–18]. More efforts should be devoted to the preparation of composite scaffolds based on natural materials.

Silk fibroin (SF) spun by the silkworm, has been widely used in

textile, skincare products, and military protection for a long time [19–22]. FDA has recently approved it as a biomedical material for regenerative medicine [23–25]. The structure of SF is mainly composed of hydrophobic crystalline regions (GAGAGS amino acid block domains in β-sheet conformation) and hydrophilic amorphous regions (elastin-like VPGXG amino acid block domains in random coil or α-helix conformation), which endow it with good biocompatibility, mechanical strength, and biodegradability [26,27]. SF scaffolds, including some approved or clinical trial scaffolds have shown reparative effect in short-distance (<10 mm) vascular injury (SDVJ) defects. For LDVJ, however, it is easy to be degraded before the blood vessel is remodeled completely, resulting in some unexpected effects, such as vascular wall perforation and thrombosis. To solve the above problems, the novel composite materials based on SF have been widely developed [28,29].

Due to their unique magnetic properties, magnetic nanoparticles (MNPs) have been extensively used in biological engineering, such as drug delivery and cell labeling [30–32]. Perea et al. [33] found that radial magnetic force can immediately drive MNPs-labeled cells onto the luminal surface of a tubular scaffold and promote cell attachment, which significantly enhanced the repair of blood vessels. Moreover, the repaired blood vessels can also be observed in real-time after magnetic scaffold transplanted through magnetic resonance imaging (MRI) technology, thus realizing triple effect: improved performance, anti-thrombosis, and real-time observation. In this study, we constructed a novel composite scaffold by loading different concentrations of MNPs into SFC. The physical and chemical properties of MSFCs were characterized by scanning electron microscope (SEM), energy dispersive spectroscopy (EDS), Fourier transfer infrared (FTIR), X-ray diffraction (XRD), X-ray photoelectron spectroscopy (XPS), thermogravimetric analyzer (TGA), and differential scanning calorimetry (DSC). The mechanical properties, magnetic response performance, and degradation *in vitro* and *in vivo* of the scaffolds were studied. The introduction of MNPs can improve the magnetic response and mechanical properties of SFC. And the delayed degradation can be obtained because of the newly formed hydrogen bonds between SFC and MNPs, which improves crystallinity and inhibits the synergistic effect of protease. Furthermore, the macrophages can gradually phagocytize MNPs without affecting their normal physiological functions. The appropriate amount of MNPs can upregulate the secretion of cytokines. The high safety and suitable degradation performance of MSFCs have been verified by the *in vitro* cell experiments and *in vivo* transplantation. MSFCs are found to promote the proliferation of vascular endothelial cells (VECs), which could be used as a potential material for long-distance vascular repair.

2. Materials and methods

2.1. Materials

The natural mulberry silk fibers were purchased by Xinyuan Cocoon Products Co., Ltd (Haian, Jiangsu Province, China). The magnetic nanoparticles (MNPs or γ-Fe$_2$O$_3$@Polydextrose sorbitol carboxymethyl ether, PSC; 25 mg/mL; ultrapure water as a solvent; PSC was a network film coated on the surface of the γ-Fe$_2$O$_3$ with the particle size of about 19–31 nm were provided by Jiangsu Key Laboratory for Biomaterials and Devices (Figs. S1A–C), which were prepared with hydrocooling, and magnetically internal heating coprecipitation method [34]. The anhydrous sodium carbonate and absolute ethanol were obtained from Sinopharm Chemical Reagent Co., Ltd, China.

2.2. Preparation of MSFCs

Mulberry silk fibers were first soaked in Na$_2$CO$_3$ solution (w/v, 0.5%, Sinopharm Chemical Reagent) (silk fibers/Na$_2$CO$_3$ solution = 1/50, w/v), then heated to boiling for 30 min. The silk fibers were washed three times with deionized water after degumming. The above steps were repeated three times until the detergent was neutral. Then the excess

water was wrung out and dried on a clean bench. When the silk fibers were completely dried, it was dissolved in H$_2$O/ethanol/CaCl$_2$ (mole ratio = 8/2/1) solution at 72 °C for 40 min under stirring condition (for 20 g of degummed silk fibers, about 85 mL of H$_2$O/ethanol/CaCl$_2$ solution was added). The silk fibroin solution was cooled and dialyzed in a dialysis bag (12000–14000 Da MW cutoff, Yuanye Biotechnology Co., Ltd, China) with deionized water for three days. Finally, the dialysis solution was concentrated to 8% (w/v) at room temperature in the fume hood. Then the lyophilized porous scaffolds were prepared according to the previous literature description [35]. Briefly, the concentrated SF solution was slowly added to the culture plate with no visible bubbles. The culture plate was transferred to an automatic freeze-drying machine and kept freeze-drying for 36 h. After 36 h, the SFC in the culture plate was removed and immersed in anhydrous ethanol for 14 h to make the branch structure change from α-helix to the β-sheet structure. The SFC with micron-sized dimensions was successfully prepared. The porous SFC was immersed entirely in solutions with different concentrations of MNPs for 24 h to maintain the full absorption and uniform distribution of MNPs in the scaffold's inner structure. After removing the excess MNP solution in the scaffold by filter paper, it was transferred to the automatic freeze-drying machine again and freeze-dried for 36 h to obtain the MSFCs (Fig. S1D). The sample codes and abbreviations of scaffolds were shown in Table 1.

2.3. Morphological observation

A scanning electron microscope (SEM, Ultra Plus, Zeiss, Germany) with energy dispersive spectroscopy (EDS) was used to study the existence of MNPs in the SFC. Besides, SEM was also used to understand the distribution of MNPs in the scaffold and internal structure morphology. The scaffolds for observing the internal structure were first placed on a conductive paste, and a layer of gold nanoparticles was sputtered with a vacuum coating machine to enhance the conductivity of scaffolds, and then the images were collected. According to the SEM images, 30 holes were randomly selected to measure the diameter through the ImageJ software. The rest of the samples used for SEM observation did not need to be sprayed with gold.

2.4. Porosity

The scaffold's porosity (ε) was measured by n-hexane as a replacement liquid in five replicates per scaffold. The scaffolds were separately immersed in a graduated centrifuge tube containing a definitive volume of n-hexane (V1) at room temperature. Moreover, the volume of liquid containing the immersed sample was defined as V2. The remaining volume of n-hexane after removing the sample was taken as V3. The porosity was calculated by the following equation (1):

$$\varepsilon\ (\%) = (V1–V3)/(V2–V3) \times 100\% \tag{1}$$

Table 1
Sample codes and abbreviations of scaffolds.

Samples	Abbreviation	MNPs concentration (μL/mL)
SF scaffold	SFC	0
SF scaffold with MNPs (composite scaffold), MSFCs		
SF scaffold with MNPs-1	MSFC10	10
SF scaffold with MNPs-2	MSFC50	50
SF scaffold with MNPs-3	MSFC100	100
SF scaffold with MNPs-4	MSFC150	150
SF scaffold with MNPs-5	MSFC250	250

Notes: 1. MSFC10, MSFC50, MSFC100, MSFC150 and MSFC250 were collectively referred to as MSFCs; 2. SFC, MSFC10, MSFC50, MSFC100, MSFC150 and MSFC250 were collectively referred to as scaffolds of different scaffolds.

2.5. Fourier transform infrared spectroscopy (FTIR)

The FTIR spectra of the SFC, MSFC10, MSFC50, MSFC100, MSFC150, MSFC250 (in the form of KBr flakes) were analyzed using a Bruker TENSOR 27 spectrometer (Germany) in the range of 4000 cm^{-1} to 400 cm^{-1} at a resolution of 4 cm^{-1} with 128 coadded scans. The spectra data collection and processing were using OPUSTM software. Amid I band deconvolution was done for each spectrum to measure the crystallinity (β-sheet content) using PeakFit 4.0 software according to previous studies [36,37]. It should be noted that each spectrum reported in this article was from a single experiment, which only represented the result of the second derivative of a spectrum. However, the data obtained from the spectra reported in this article (such as the content of the second structure) were the average results of at least three individual samples.

2.6. X-ray diffraction (XRD)

The XRD patterns of the SFC, MSFC10, MSFC50, MSFC100, MSFC150, MSFC250 were tested using an advanced XRD diffractometer (Ultima IV, Japan) at a radiation wavelength (γ = 0.154 Å) at a beam energy of 40 kV and a current of 40 mV with a scanning rate of 5°/min (2θ = 10–45°).

2.7. X-ray photoelectron spectroscopy (XPS)

The XPS (Thermo ESCALAB 250XI, USA) was used to investigate the elemental composition and chemical state of scaffolds ranging from 1300 to 0 eV. The high-resolution spectra of Fe2p, C1s, N1s, and O1s were also recorded. The data analysis was performed by using XPSPEAK software provided by the manufacturer.

2.8. Nuclear magnetic resonance (NMR)

The ^{1}H NMR of SFC, PSFC (Abbreviation of PSC with SFC), MSFCs, PSC were tested to observe hydrogen bonds by an NMR spectrometer (Bruker Avance III HD 600 MHz, Germany) using a 5 mm Z gradient field forward multi-core broadband two-in-one liquid probe. All samples to be tested were prepared by dispersing them uniformly in D$_2$O and maintaining them at 37 °C for 24 h.

2.9. Thermal properties

The thermal properties of SFC and MSFCs were detected by Thermogravimetric analyzer (TGA800, Perkin Elmer, USA) with a heating step of 20 °C/min, range of 30–800 °C, and differential scanning calorimetry (DSC4000, Perkin Elmer, USA) with a heating step of 10 °C/min, and range of 30–350 °C. The samples were individually grounded into a powder and placed in a fixed aluminum plate for testing.

2.10. In vitro degradation

All dried scaffolds were weighed and recorded as W1. Each scaffold was weighed five times in succession. Each scaffold was completely immersed in 0.5 mg/mL protease XIV (≥3.5 U/mg; Sigma-Aldrich, Proteolytic enzyme) PBS solution on a 37 °C shaker with 150 rpm/min. The fresh enzyme solution was replaced every two days to maintain protease vitality. The PBS (0.01 M, pH 7.40) without protease XIV was set as the control group with the same steps. After a predetermined time, the wetted scaffold was washed five times with deionized water and then put into the freeze-drying machine for sample drying. The products were weighed as W2. Five parallel samples were measured for each scaffold. The remaining weight was calculated by the following equation (2):

$$\text{Weight remaining (\%)} = \text{W2/W1} \times 100\% \qquad (2)$$

2.11. Mechanical properties

The mechanical strength of the SFC and MSFCs was measured in wet conditions with an electronic universal testing machine UTM107 system software (Junping Equipment Co., Ltd, Yangzhou, China). The crosshead speed was 2 mm/min at room temperature. The maximum-load, maximum load elongation, maximum load displacement, tensile strength, breaking strength, and elastic modulus were determined. Five samples were measured for each scaffold.

2.12. Swelling behavior

The PBS (or ddH$_2$O or DMEM) was used as displacement liquid for swelling rate detection. The dried scaffolds were weighed separately as W1 and then immersed in PBS (or ddH$_2$O or DMEM) in a 37 °C water bath for 24 h. The wetted scaffolds containing PBS (or ddH$_2$O or DMEM) solution were removed from displacement liquid, and the weight was set as W2. Five parallel samples were measured for each scaffold. The swelling ratio was calculated by the following equation (3):

$$\text{Swelling ratio (\%)} = \text{(W2–W1)/W1} \times 100\% \qquad (3)$$

2.13. Magnetic properties

The hysteresis loop represented the magnetic response of the MSFCs was evaluated using a vibrating sample magnetometer (VSM, 7407 Lakeshore, CA) from -10000 to 10000 Oe. The MSFCs were grounded into a fine powder, coated on a weighing paper, and attached to a vibrating rod for measurement with a ±0.5% magnetization error. The magnetocaloric effect was measured by a moderate radio frequency heating machine (SPG-10-II, Shenzhen, China) at an operating frequency of 1.5 MHz and a current of 15 mA within 600 s. The scaffolds were grounded into a fine powder and placed in a 1.5 mL Eppendorf (EP) tube for experimental testing.

2.14. Protein concentration test

The effect of MNPs on SFC's degradation was assessed by BCA Protein Assay Kit (KGPBCA, KeyGEN BioTECH, Jiangsu, China). Briefly, a 40 mg scaffold was placed in 15 mL graduated centrifuge tubes (5 mL PBS, 0.01 M, pH 7.40) containing 0.5 mg/mL protease XIV (≥3.5 U/mg; Sigma-Aldrich, Germany), and then transferred into a shaker (150 rpm/min) at 37 °C for one week. The fresh enzyme powder was added every two days to maintain protease vitality. After one week, the sample was centrifuged (8000 rpm/min), and the protein concentration of the supernatant was detected. Besides, we also set up another set of experiments without protease XIV in the same steps as above. Five parallel samples were measured for each scaffold.

2.15. Fluorescence spectroscopy

To prove that the iron atoms in MNPs might be complexed with tyrosine residues to reduce protein activity in the protease XIV solution, we used fluorescence spectroscopy to collect specific fluorescence absorption peaks. The spectra were recorded for all samples by a Fluorescence Spectrometer (Flouro-Max-4, HORIBA, Kyoto, Japan). The fluorescence was excited at 275 nm, and the emission was recorded in the range of 280–400 nm with excitation (EX) and emission (EM) slits with a 5 nm resolution.

2.16. Protease activity test

To explore the interaction between iron atoms in MNPs and the tyrosine (active center) in protease XIV (SLCB5967, Sigma-Aldrich,

America), the activity of the protease XIV solution activity was detected by a Folin-Ciocalteu method. Briefly, a tyrosine standard curve was first established by the specific standard solution configuration method, as shown in Table S1. After mixing, the standard solution was transferred to a water bath and incubated for 30 min at 37 °C. Then the absorbance of the tyrosine standard was measured at 660 nm by a fully automatic microplate reader. The formula for calculating the standard curve of tyrosine was as the following equation (4):

$$\Delta A\ _{Standard} = A\ _{Standard} - A\ _{Standard\ Blank} \tag{4}$$

For the MNP groups, we used the same concentration of protease XIV ($\geq$3.5 U/mg) PBS solution (0.5 mg/mL) as the degradation experiment. Then the MNPs were added to the protease solution and transferred to 37 °C shaker incubation. Samples were tested at predetermined time points (0, 6, 12, 24, 32, and 48 h) at 660 nm by a fully automatic microplate reader. To eliminate the color interference of MNPs, we set all MNP groups at 0 h as a blank sample. Since the MNPs were coated with a PSC, we also set the PSC groups' equal content without containing γ-Fe$_2$O$_3$. Three parallel samples were tested for each group of samples. The formula for calculating the protease activity was as equation (5):

$$\Delta A\ _{Sample} = A\ _{Test} - A\ _{Sample\ Blank} \tag{5}$$

The μmoles of Tyrosine equivalents liberated were determined by using the standard curve called as m.

$$u = \frac{(m)(1)}{(2)(3)(4)}$$

u = Units/mL protease
1 = Total volume (in milliliters) of assay
2 = Time of assay (in minutes) as per the Unit Definition
3 = Volume of protease (in milliliter) of protease used
4 = Volume (in milliliters) used in Colorimetric Determination

$$U = \frac{u}{m}$$

m = mg solid/mL protease
U = Unit/mg solid

2.17. MNPs releasing test

All dried pure SFCs were prepared to refer to *method 2.2*, and then immersed entirely in solutions (10 mL) with different concentrations of MNPs for 24 h and taken out. The total MNPs content of the solution minus the remaining liquid MNPs content after soaking was the content of MNPs absorbed by the scaffold. The obtained dried MSFCs were transferred to a 50 mL centrifuge tube with ultrapure water (or PBS or DMEM) release solution (20 mL) on a 37 °C shaker with 150 rpm/min. After a predetermined time (24, 48, 72, 96, 120 h), the release solution (1 mL) was drawn for Fe content detection by an inductively coupled plasma atomic emission spectrometry (ICP-AES). When the second time point was reached, the Fe content of the released liquid was tested again, and the Fe content absorbed at the first time point was added, which was the amount of MNPs released at the second time point. The release of MNPs at each time point followed the above method. The ratio of the content of MNPs in each release solution to the total MNPs absorbed by the scaffold at each time point was the percentage of MNPs released. Three parallel samples were measured for each scaffold at each time point.

2.18. Prussian blue staining

The scaffolds first were obtained through a 24-well culture plate containing 500 μL of silk fibroin solution and sterilized by ethylene

oxide. Subsequently, the macrophage (RAW264.7) suspension with a density of 5×10^4 cells/well was seeded into a 12-well culture plate for 12 h in a 37 °C humid atmosphere with 5% CO$_2$, and then the scaffolds obtained above were soaked into the culture medium and cultured continuously for 24 h. Next, the cell suspension and scaffolds were removed and fixed with 4% paraformaldehyde for subsequent Prussian blue staining and F-actin staining. Briefly, the cell culture plate obtained above were washed with PBS (pH 7.40, 0.01 M) three times, then co-incubated containing 200 μL of Prussian blue dye (v/v = 1: 1, G1422, Solarbio, China) per well for 30 min at room temperature in the dark. After incubation, the Prussian blue dye was removed and washed once with PBS, and then the optical image of the cell was obtained under an optical microscope.

2.19. F-actin staining

To evaluate whether the released MNPs being phagocytosed by macrophages would affect the state of macrophages. The F-actin expression was evaluated by phalloidin-FITC staining. Briefly, the cell culture plate obtained above (*Materials and methods 2.18*) were washed with PBS three times, then co-incubated containing 200 μL of phalloidin-FITC dye (v/v = 1: 40, CA1620, Solarbio, China) per well for 1 h at room temperature in the dark. After incubation, the phalloidin-FITC dye was removed and washed with PBS three times, and then the F-actin image of the cell was observed under a fluorescence microscope. The obtained fluorescence microscopy images were quantitatively measured by ImageJ software.

2.20. Live/dead cell staining

All cell culture steps refer to *Materials and methods 2.18*, and only the seeding density was modified to 1×10^5 cells/well. Briefly, the cell culture plate obtained above were washed with PBS three times, and then the live/dead cell dye (R37601, Thermo Fisher Scientific, Germany) was added to the culture plate and incubated in a 37 °C humidified environment with 5% CO$_2$ for 30 min. After staining, the cell culture plates were washed with PBS three times, and then the stained cells were observed by a fluorescence microscope, where the living cells showed green while the dead cells showed red. The statistical analysis was performed through ImageJ software.

2.21. Cytokines expression test

Macrophages phagocytosed the MNPs released from the MSFCs. Whether it would affect the change of cytokine expression was evaluated by the ELISA experiment. The cell suspension was collected from *Materials and methods 2.20*. Then transferred to a centrifuge (12000 rpm/min) for 5 min, and the supernatant was collected again. Cell cytokines were quantified by the ELISA kit, and three parallel samples were set in each assay. All ELISA kits were purchased from MEIMIAN in China. All samples must be established with standard concentration curves according to the ELISA kit requirements before testing.

2.22. Cytotoxicity test in vitro

The scaffolds were first to cut into 20 μm slices using a microtome, adhered to cell slides, and sterilized by ethylene oxide. The complete medium containing Dulbecco's modified Eagle medium (DMEM, Gibco) with 10% fetal bovine serum (FBS, Gibco) and 1% penicillin-streptomycin (PS, Gibco) was obtained by immersing scaffolds in a 12-well culture plate. The human umbilical artery vascular smooth muscle cells (HUASMC) were seeded into a 12-well culture plate with a density of 2.5×10^4 cells/well and incubated at 37 °C in a humidified air containing 5% CO$_2$. After the medium was removed at a predetermined time (1, 2, 3 d), the optical microscope observation, cytoskeleton morphology fluorescence staining, and CCK-8 cell viability were

studied.

The effect of the scaffolds on the HUASMCs cytoskeleton system was observed by phalloidin-FITC immunofluorescence staining. After removing the medium, fixed it with 4% paraformaldehyde for at least 15 min, and the samples were rinsed with detergent (P0106, Beyotime, China) three times with 5 min each. The HUASMCs were then permeated with Triton-100 (0.5%, v/v) for 10–15 min and were rinsed with detergent three times again. The HUASMCs would be co-incubated with phalloidin (1: 40, v/v, Solarbio, China) for 20–30 min at room temperature under a dark condition. After incubation, the phalloidin staining solution was gently removed and washed once with detergent, and then the fluorescence images were collected by a fluorescence microscope.

After removing the medium, the complete fresh medium mixed with CCK-8 solution (v/v = 10/1, 500 μL/well) was supplemented and then co-incubated for 4 h. Afterward, the incubation solution (200 μL) was transferred into a standard 96-well plate, and the absorbance was measured at 450 nm by a fully automatic microplate reader.

2.23. Hemolysis test

All animal experiments were performed according to the Guidelines for Care and Use of Laboratory Animals established by Medical School of Southeast University Institutional Animal Care and Use Committee. The stroke-bearing protocol was approved by the Committee on the Ethics of Animal Experiments of Medical School of Southeast University (Ethical Lot Number: 20190307011). The hemolytic test was tested by taking blood from the heart of New Zealand rabbits (2.0–2.5 kg, female). Briefly, a blood sample was added to sodium heparin (3.8%, w/v) to prevent blood coagulation, and then a physiological saline solution was added to the blood sample (v/v = 4: 5). Then it was diluted as a stock solution. The scaffold samples (SFC and MSFCs, 50 mg per scaffold) were placed in a 1.5 mL EP tube with physiological saline (1 mL), and the mixture was placed in a water bath at 37 °C for 30 min. Besides, the distilled water and physiological saline were used as a positive control and negative control, respectively. Finally, each EP tube was filled with a rabbit bloodstock solution (100 μL) and then incubated at 37 °C for 1 h. After centrifugation, the absorbance was determined at 540 nm by a fully automatic microplate reader. The formula for calculating the hemolysis rate of the composite scaffold sample was as equation (6):

$$\text{Hemolysis rate (\%)} = [(OD_t - OD_P)/(OD_P - ODn)] \times 100 \qquad (6)$$

Where OD_t was the absorbance of the scaffold samples, OD_P was the absorbance of the positive control, and ODn was the absorbance of the negative control.

2.24. In vivo implantation of SFC and MSFCs in rabbits

All animal experiments were performed according to the Guidelines for Care and Use of Laboratory Animals established by Medical School of Southeast University Institutional Animal Care and Use Committee. The stroke-bearing protocol was approved by the Committee on the Ethics of Animal Experiments of Medical School of Southeast University (Ethical Lot Number: 20190307011). The female New Zealand rabbits with a weight of 2.0–2.5 kg were used to be implanted by scaffolds. The rabbits were first anesthetized with 3% (w/v) sodium pentobarbital. Then the sterilized scaffolds (SFC, MSFC10, MSFC250) were transferred to the rabbit's back. The rabbits were sacrificed at predetermined time points (1 W, 2 W, 4 W, 16 W), and the degraded scaffolds were collected. The degraded scaffolds removed from the backs of three rabbits were put into physiological saline for *in vivo* degradation study, and the degraded scaffolds taken out from the other three rabbits were fixed with 4% paraformaldehyde for tissue sectioning.

The degraded scaffolds used for *in vivo* degradation were processed. Briefly, the connective tissue on the surface of the degraded scaffolds

was carefully peeled by an ophthalmic scissor and then repeatedly washed with deionized water. The degraded scaffolds were treated in a 500 U/mL collagenase solution and a 5 mg/mL trypsin solution at 37 °C for 24 h, respectively, followed by rinsing with deionized water five times, and then washing with 1% Triton X-100 for 24 h. In the process, the fresh solution was changed every 3 h and repeatedly washed with deionized water. Finally, the processed scaffolds were dried in a 60 °C oven until constant weight to check the degradation *in vivo*. Besides, the paraformaldehyde-fixed material was sliced through a frozen microtome. The acute inflammatory response was observed by hematoxylin and eosin (H&E) staining.

2.25. Immunofluorescence staining

The obtained tissue sections (10 μm sheet thickness) were also co-incubated with primary CD14 (1: 200) antibody (Rabbit Polyclonal, proteintech, China) overnight at a 4 °C refrigerator. After washing with detergent (P0106, Beyotime, China) three times for 5 min, the samples were co-incubated again with Cy3 secondary antibody (1: 50, SA00009-1, proteintech, China) and dark atmosphere overnight at a 4 °C refrigerator. The samples were observed by a fluorescence microscope.

2.26. Immunohistochemistry staining

The obtained tissue sections (10 μm sheet thickness) were co-incubated with primary CD34 (1: 200) antibody (Rabbit Polyclonal, proteintech, China) overnight at a 4 °C refrigerator. After washing with detergent (P0106, Beyotime, China) three times for 5 min, the samples were co-incubated again with an HRP-conjugated secondary antibody (1: 500, ab6721, Abcam, Cambridge) for 60 min at room temperature. The expression was observed with 3, 3-diaminobenzidine (DAB) staining.

2.27. Statistical analysis

All quantitative data were expressed as the mean ± standard deviation (SD). Differences between the two groups were inspected by using a paired Student's t-test, and a comparison of multiple groups was performed by one way of variance (ANOVA). The results were considered significant at $*P < 0.05$, $**P < 0.01$, $***P < 0.001$, $****P < 0.0001$, $n \geq 3$.

3. Results

3.1. Morphological characterization and analysis

To demonstrate that MNPs of different concentrations were successfully and uniformly loaded into the SFC, the EDS analysis (Fig. 1A) showed that SFC as the control group did not appear the absorption peak of Fe, while the MSFCs groups appeared the absorption peak of Fe. Moreover, the absorption peak became more prominent with the increase of MNPs concentration. Fig. 1B–C showed the SFC and MSFCs' surface morphology and evenly assigned an area on the surface for EDS analysis. The mass percentage and atomic percentage of Fe were negative, which indicated that the SFC did not contain Fe element, while the surface morphology of MSFC had many nanoparticles-like protrusions, and non-protruding regions and granular protruding regions were selected for EDS elemental analysis. The results showed that Fe was not detected in the non-protruding regions, while the weight percentage and atomic percentage of the granular protruding regions were 11.24% and 2.93%, respectively. These results indicated that the MSFCs were successfully prepared. To further investigate the distribution of MNPs in the scaffold, MSFC10 and MSFC250 samples were selected for high-magnification SEM image acquisition (Fig. 1D). The results showed that the sparse gray dots with an average diameter of 27.64 nm were uniformly distributed on the surface of MSFC10, while the gray dots of
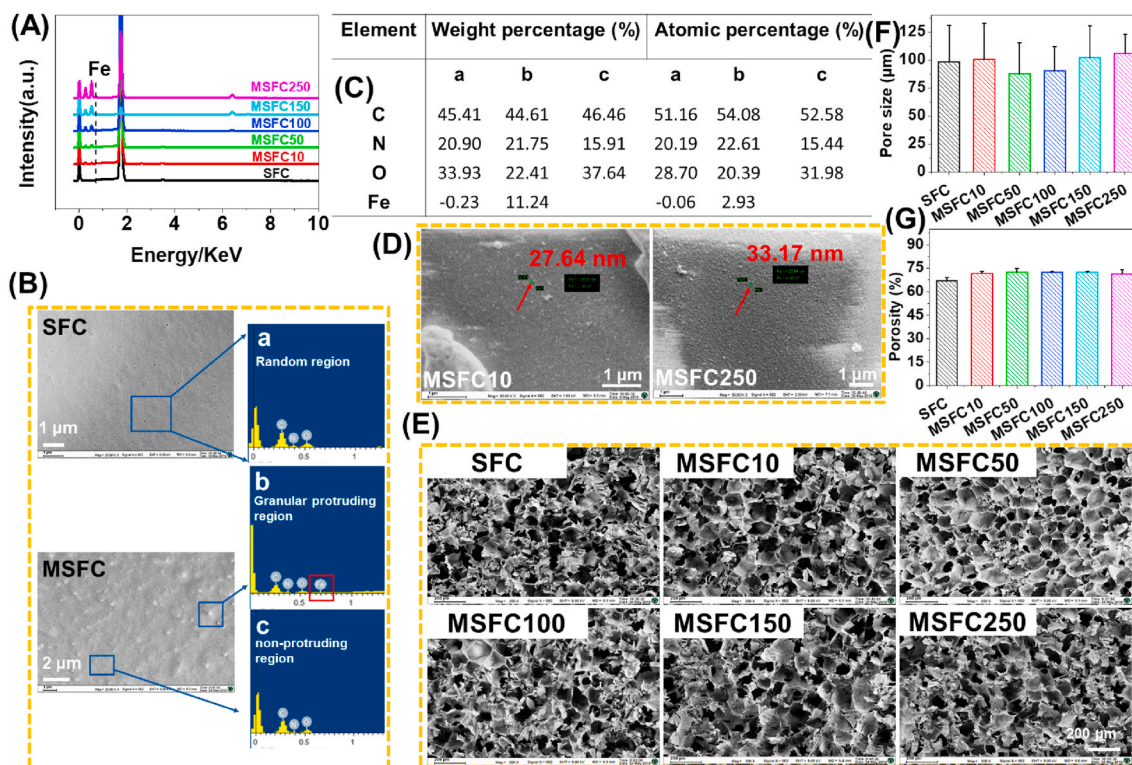
Fig. 1. (A) The energy dispersive spectroscopy (EDS) spectrum of SFC and MSFCs; (B) SEM-EDS result of SFC and MSFC50 and (C) statistical results of the EDS; (D) SEM images of MNPs distribution in the MSFC10 and MSFC250; (E) The SEM micrographs of SFC and MSFCs; (F) The pore size of SFC and MSFCs, n = 30; (G) The porosity percent of SFC and MSFCs, n = 5.

MSFC250 were denser with 33.17 nm in diameter, showing the better distribution state of MSFC250.

The structural morphology of all scaffolds was observed by SEM. As shown in Fig. 1E, all scaffolds presented a continuous network of porous structures. Fig. 1F showed the average pore size of all scaffolds. The pore size of SFC was 98.71 ± 32.63 μm, whereas that of MSFC10, MSFC50, MSFC100, MSFC150, MSFC250 samples was 100.53 ± 32.10, 87.90 ± 27.54, 90.21 ± 21.84, 102. 46 ± 27.99, 105.97 ± 16.99 μm, respectively. The pore size of MSFC50 and MSFC100 exhibited relatively smaller pore size than MSCF10, MSFC150, MSFC250 (like to SFC pore size). The MSFC50 showed the smallest pore size distribution. The porosity of all samples was presented in Fig. 1G. The porosities ranged from about 67.09 to 72.60%, and there was no significant difference between the scaffolds.

3.2. FTIR, XRD, XPS and NMR analysis

The FTIR spectra were conducted to analyze the MSFCs composition. It was presented in Figs. 2A and S2A. Peaks at 1010 cm^{-1} and 1046 cm^{-1} assigned to -C-O-C- vibration were evident of ether bond in MNPs and MSFCs. It validated the successful construction of SFC complexing with MNPs. The characteristic absorption peak of SFC was observed at 3293 cm^{-1}, which represented the stretching vibration of the peptide bond (-CONH-) of SFC, which was consistent with the MSFCs. Besides, the specific peaks also were observed at 1625 cm^{-1} (amide I, C=O), 1523 cm^{-1} (amide II, N–H), 1235 cm^{-1} (Amide III, N–H or C–H), which represented β-sheet of the SFC. Compared with the SFC control group, the peaks of MSFCs in the amide I, II, III regions all showed an enhancement tendency, indicating an increase of β-sheet content. According to previous studies [38], hydrogen bonding between the carboxyl and amino groups (C=O–H–N) existed in the three amide regions. Such a combination was simple and effective in strengthening the structure of the scaffold. Due to the addition of MNPs, the infrared

absorption peaks of the three amide regions were enhanced, which might be attributed to the participation of MNPs in the conformational transition of SFC. The amide hydrogen bond was strengthened by the content increase of the SFC β crystal structure, indicating that MNPs participated in SFC's conformational transformation. To further verify that MNPs were indeed involved in SFC's conformational transition, peak deconvolution analysis was performed (1600-1700 cm^{-1}) and was shown in Fig. 2B. The composition of the secondary structure was measured for each scaffold accordingly (Fig. 2C and Table S2). The percentages of SFC secondary structure as the control group were 37.80% for β-sheet, 46.00% for random coil or helix, and 16.20% for β-turn. The percentages of MSFC10 changed as 39.00% for β-sheet, 44.60% for random coil or helix, and 16.40% for β-turn. The percentages of MSFC50 changed as 39.80% for β-sheet, 45.80% for random coil or helix, and 14.40% for β-turn. The percentages of MSFC100 changed as 41.40% for β-sheet, 43.90% for random coil or helix, and 14.70% for β-turn. Furthermore, the percentages of MSFC150 changed as 42.80% for β-sheet, 41.10% for random coil or helix, and 16.10% for β-turn. Finally, the secondary structure percentage of MSFC50 with the highest MNPs changed to 44.90% for β-sheet, 40.00% for random coil or helix, and 15.10% for β-turn. These data indicated that MNPs were indeed involved in the conformation transition of SFC. In particular, the content of β-sheet, which determined the physical properties of SFC, showed a significant gradient increase with the increase of MNPs. It might also be a major mechanism for the following enhancement of mechanical properties and delayed degradation.

To further demonstrate the β crystal structure change of MSFCs, XRD analysis was performed. Fig. 2D showed the XRD pattern of MSFCs. As a control group, the SFC peak appeared at 21.85°, representing α-helical or random coils structures. In contrast, the peak of MSFC50 located at 20.37° was assigned to β-sheet structures. It indicated that the conformation changed from α-helical and random coils structures to β-sheets under the influence of MNPs. More importantly, the SFC's crystal
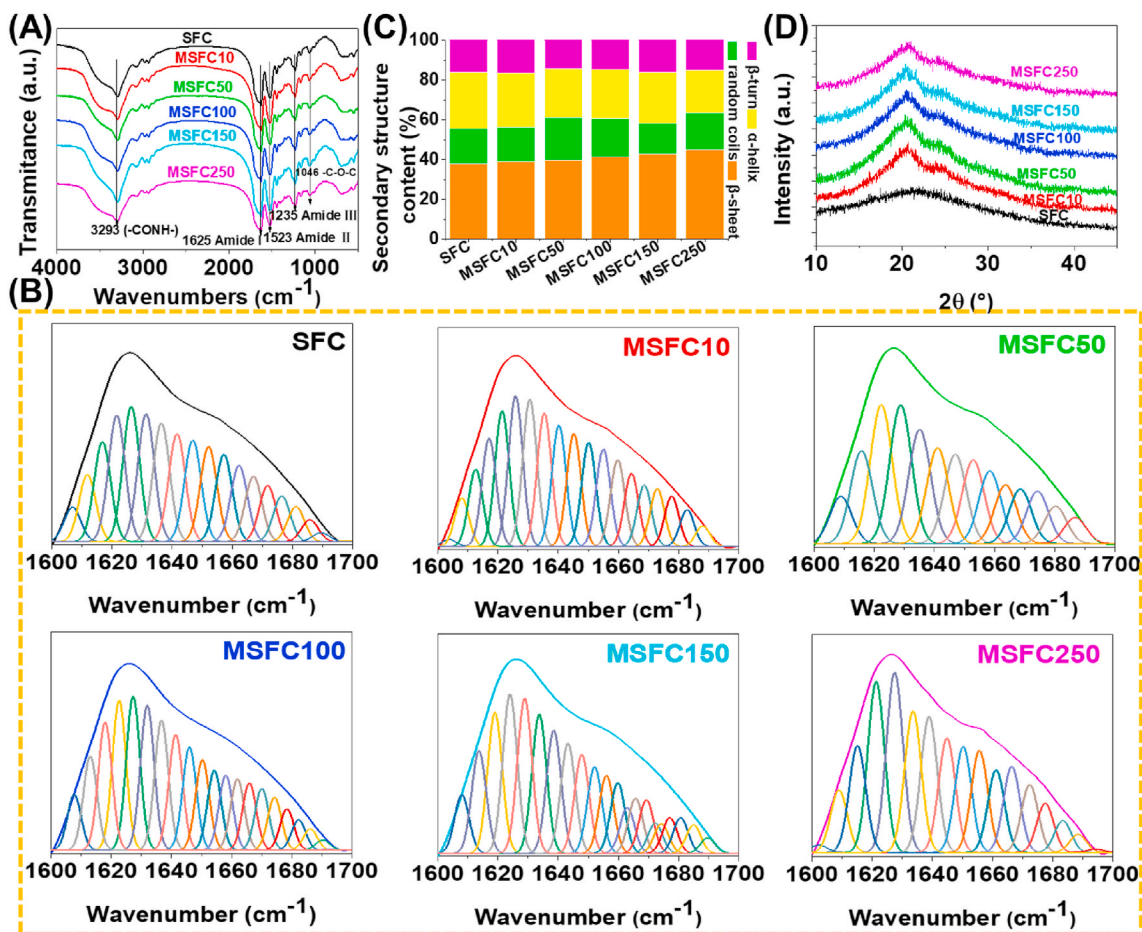
Fig. 2. (A) The FTIR spectrum of SFC and MSFCs; (B) Deconvoluted FTIR spectra of the amide I band (1600-1700 cm^{-1}) of SFC and MSFCs; (C) Comparison of the secondary structures of the SFC and MSECs, n = 3; (D) The XRD spectrum of SFC and MSFCs.

structure was strengthened by the addition of MNPs, which was consistent with the FTIR results.

The elemental composition and the chemical state of MSFCs (only MSFC50) were also analyzed by XPS. Fig. S2B showed three typical signal peaks representing C 1s at 284 eV, N 1s at 398 eV, O 1s at 528 eV for both SFC and MSFC50. In contrast, a unique Fe 2p signal peak was observed in MSFC50. It indicated that the MSFC50 was mainly composed of C, N, O, and Fe elements. To further observe the chemical state at MSFC50, high-resolution XPS spectra were performed. It could be seen from Fig. S2Ci showed that SFC did not have any signal peak, and MSFC50 presented two atomic orbital valence states of Fe containing o-Fe$_{2p3/2}$ and o-Fe$_{2p1/2}$. As shown in Fig. S2Cii-iv, the binding energy of the C 1s, N 1s, and O 1s atomic orbitals in MSFC50 was higher than that of SFC, which indicated that MNPs promoted electron transfer in the three orbitals. The binding also indicated that there was a chemical interaction between SFC and MNPs, which was consistent with the results of FTIR.

Fig. S3showed 1H NMR spectra of SFC, PSFC, PSC (PSC came from the surface of MNPs). The MSFCs had no peaks because of the interference of magnetic particles (γ-Fe$_2$O$_3$), so the 1H NMR of MSFCs was not presented. As shown in the 1H NMR spectra, the different chemical environments of H in the SFC were indicated in the 1H NMR spectra of SFC and PSFC. From the 1H NMR spectra of PSFC, we could observe all the different chemical environments of H in the SFC. In addition to the different chemical environments of H in the SFC, the new peak of 1H NMR was also observed in the 1H NMR spectra of PSFC, and the chemical shift was also observed between PSFC, SFC, and PSC. These results indicated that PSC was successfully conjugated onto the

molecular chain of SFC, which was consistent with that of FTIR and XPS spectra of PSFC.

3.3. Thermal and magnetic analysis

The thermal stability of MSFCs was analyzed by TGA, and the TGA curves were shown in Fig. 3A. The TGA curves showed a continuous heavy loss process at 30–800 °C. The weight loss of the first step at 30–120 °C was mainly due to the evaporation of free water and combined water, and the high-resolution TGA curves indicated no significant differences in all samples at this step. In the second step, a faster weight loss occurred from 250 °C, which might be attributed to the decomposition of the SFC network structure, with the maximum weight loss rate occurring at around 295 °C. The degradation in a wide range of ~350 °C might be attributed to the oxidative decomposition of organic skeleton or C–C backbone of SFC and the decomposition of PSC organics wrapped by MNPs. However, MSFCs had different thermal degradation curves from 350 to 800 °C. The weight loss increased with the decrease of MNPs content, which might be that the combination of γ-Fe$_2$O$_3$@PSC polymer and SFC increased the thermal decomposition temperature of the entire scaffold and protected the SFC from slowing down. The thermal studies by TGA had proved that MSFCs have higher residues at 700 °C due to the presence of MNPs compared to SFC (as control). The DSC test also confirmed the above results (Fig. 3B). The melting endotherm occurred at 288.69 °C in SFC (as control), and the MSFCs occurred at 292 °C. All these results indicated that MNPs could improve the thermal stability of SFC.

The magnetic properties of MSFCs were also measured at 20–25 °C
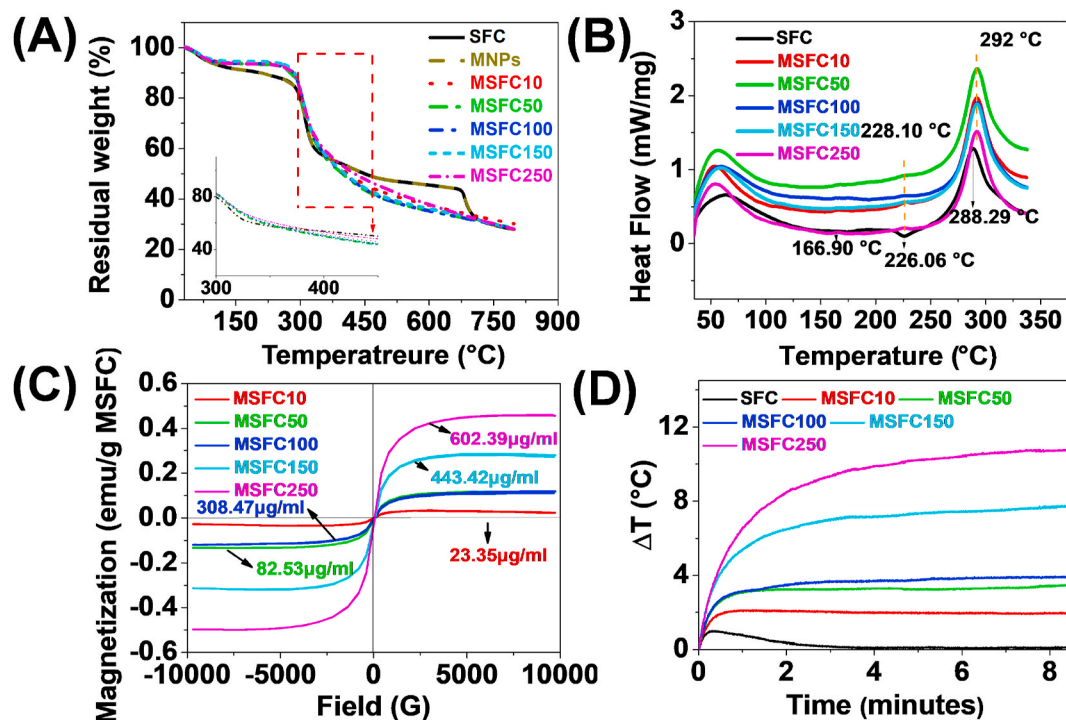
Fig. 3. Thermal analysis of SFC and MSFCs: (A) TGA curve in the range of 30–800 °C; (B) DSC curve in the range of 30–350 °C; (C) The hysteresis loop of MSFCs; (D) The curves of magnetocaloric effect with SFC and MSFCs in an operating frequency of 1.5 MHz and a current of 15 mA, $\triangle$T = Detection temperature - starting temperature.

by VSM, and the hysteresis loops were shown in Fig. 3C. It could be clearly seen that the MSFCs exhibited a good magnetic response. When applied the magnetic field ranging from −10000 to 10000 Oe, MSFCs exhibited an obvious superparamagnetism and the saturation magnetization of MSFC10, MSFC50, MSFC100, MSFC150, MSFC250) at 0.03, 0.13, 0.14, 0.30, 0.48 emu/g, respectively. It also reflected that the concentration gradient of MNPs in the scaffold was consistent with the EDS results in Fig. 1A. It meant that MSFCs could obtain effective magnetic properties with the addition of MNPs. The heating curve of the MSFCs exposed to the alternating magnetic field was recorded in Fig. 3D. As a control group, the SFC did not exhibit temperature change. The MSFCs showed a significant magnetic thermal heating effect, and the temperature increased with the increase of MNPs content. The SFC with the lowest MNPs content (MSFC10) increased about 2.00 °C while the SFC with the highest MNPs content (MSFC250) rose by up to 10.89 °C. It can also be observed that the rising temperature of the MSFC50 (3.27 °C) was very close to that of the MSFC100 (3.49 °C), which was quite consistent with the above data of saturation magnetization. Besides, the MSFC150 also exhibited a temperature rise of approximately 7.94 °C. It was demonstrated that the magnetic heating effect of the MSFCs could be controlled by MNPs content.

3.4. In vitro degradation, mechanical strength and swelling analysis

The degradation behavior of MSFCs *in vitro* was studied by immersing them in simulated enzymes *in vitro* (protease XIV). The scaffolds were also immersed in a PBS solution that did not contain protease XIV as a control. As shown in Fig. 4A, the reducing mass of all samples showed no significant change in the PBS, while SFC degraded 3.79% (the same solution system as a control). The degradation rate of MSFCs decreased with the increase of MNPs, and the highest concentration of MSFC250 samples degraded only 2%. However, all scaffolds showed significant degradation differences in protease XIV over 24 d (Fig. 4B). The SFC exhibited a maximum of 69.08% reduction mass over 24 d. The reduction mass of MSFC10, MSFC50, MSFC100,

MSFC150 and MSFC250 was 58.72%, 56.23%, 50.33%, 51.26% and 49.99%, respectively. The MSFC250 showed the lowest degradation over 24 d, which was about 20% lower than the SFC. Besides, the SFC and MSFCs were photographed at 0, 12, and 24 d respectively, and the results showed that the volume of the sample rose gradually with the increase of MNPs content, revealing the delayed degradation of the scaffold (Fig. S4). After 24 d, the structure of the inner surface and cross-section of the degraded scaffold was also observed by SEM (Fig. 4C). The results showed that the pore size of each sample group did not show significant differences except those of the MSFC150 group was significantly smallest, showing the reliability of the above results. All the results demonstrated that the degradation behavior of SFC could be regulated by MNPs concentration. The mechanical characteristics of MSFCs were measured using an electronic universal testing machine (Fig. 4Di-vi). The SFC (as control) revealed an average maximum load of 14.66 ± 0.54 N, an average maximum load elongation of 13 ± 1%, an average maximum load displacement of 0.38 ± 0.13 mm, an average tensile strength of 0.03 ± 3.33 × 10^{-3} MPa, the average breaking strength of 0.01 MPa and an average elastic modulus (Ei) of 25 ± 1 MPa. These results were consistent with previous studies on the mechanical range of SFC [39–41]. For MSFCs with different concentrations of MNPs, the mechanical strength increased with the increase of MNPs concentration. When it was raised to MSFC50, it exhibited the best mechanical strength. Its maximum load, maximum load elongation, maximum load displacement, tensile strength, breaking strength were 34.44 ± 1.30 N, 62 ± 3%, 1.85 ± 0.26 mm, 0.1 ± 0.01 MPa, and 0.11 ± 0.01 MPa, respectively. Then the mechanical strength began to decrease with the increase of MNP concentration, showing a trend of first increasing and then decreasing. From the results, it could be seen that the mechanical properties of MSFCs were higher than that of the SFC. Although the elastic modulus showed an irregular trend for MSFC10, MSFC50, MSFC100, MSFC150, MSFC250 (27 ± 1, 34 ± 2.33, 28 ± 1.33, 37 ± 3.33 MPa, respectively), it was also higher than that of SFC. The swelling test results of all scaffolds were shown in Fig. 4E. It could be seen that the SFC (as control) showed the best water absorption capacity
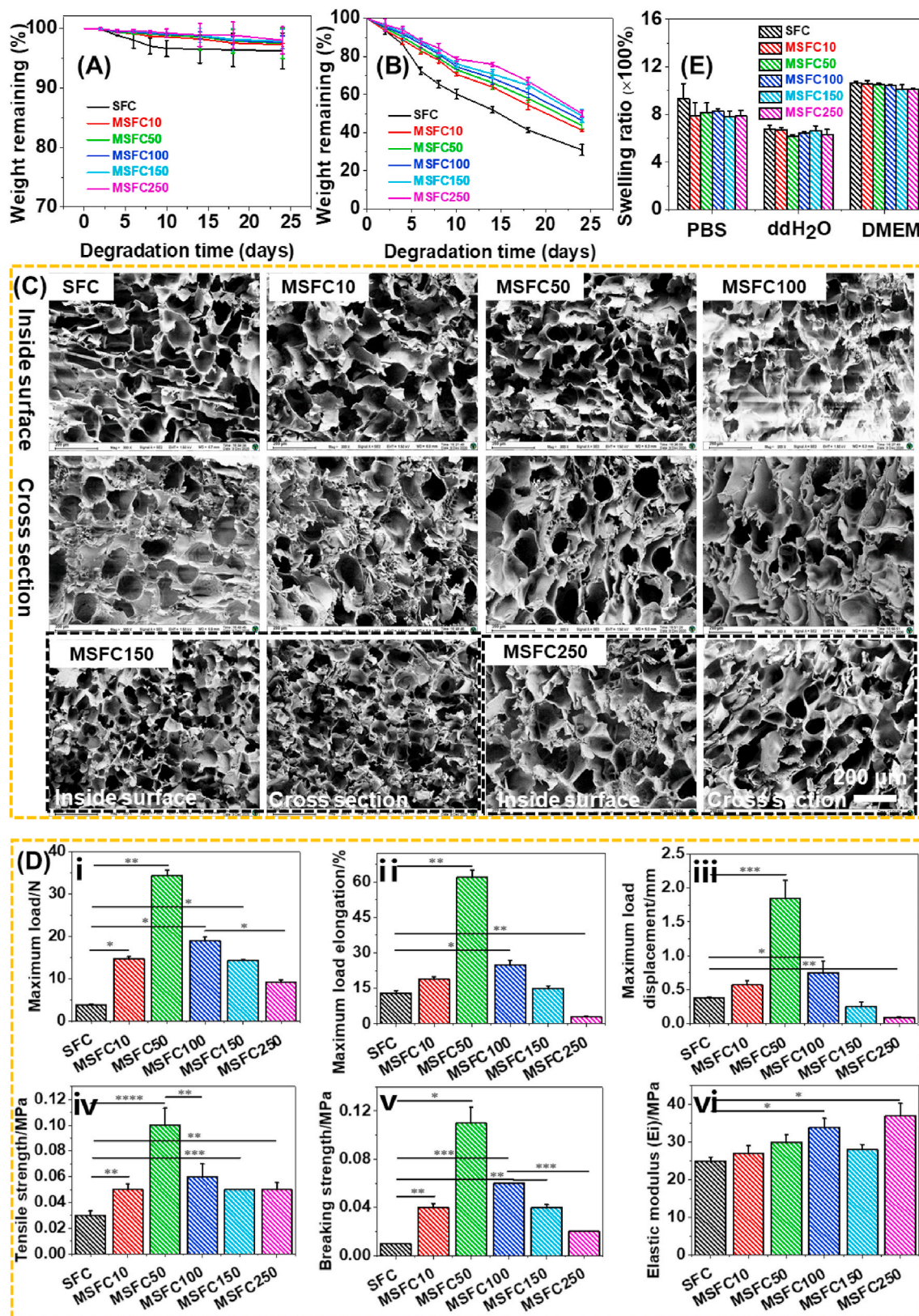
Fig. 4. *In vitro* degradation of SFC and MSFCs immersed in PBS solution, n = 5 (A) and in protease XIV solution, n = 5 (B); (C) SEM images of inside surface and cross-section of SFC and MSFCs after 24 d of degradation. (D) The mechanical strength of SFC and MSFCs containing Maximum load, Maximum load elongation, Maximum load displacement, Tensile strength, Breaking strength, Elastic modulus; n = 5. (E) The swelling ratio of SFC and MSFCs, n = 5. *P < 0.05, **P < 0.01, ***P < 0.001, ****P < 0.0001 by one-way ANOVA test.

(~931.75%), while MSFCs showed a slight decline for all MSFCs samples. The absorption capacity of MSFC10, MSFC50, MSFC100, MSFC150, and MSFC250 are ~786.90%, ~817.98%, ~828.83%, ~778.78%, and ~788.11%, respectively with no significant difference among them. The same change trend was also reflected in ddH$_2$O and DMEM. However, compared with PBS and DMEM systems, ddH$_2$O had the weakest liquid absorption capacity, while SFC still has the best liquid absorption capacity (~673.89%). The scaffolds showed the best liquid absorption capacity in DMEM in a three-phase system, and SFC (~1066.33%) showed the highest swelling rate in all samples. The water absorption capacity of the SFC was slightly higher than that of the MSFCs, possibly due to the high specific surface area of MNPs that accelerated water evaporation. However, there was no significant difference among all the experimental groups, and the MSFCs still showed good water absorption capacity.

3.5. Protein concentration, fluorescence spectroscopy and protease activity analysis

To further clarify that MNPs inhibited SFC's degradation, the protein concentration in the degradation solution was determined by BCA Protein Assay Kit. As shown in Fig. S5A, the SFC exhibited the highest protein concentration (0.28 ± 0.03 µg/µL) after one week, indicating that the SFC had the fastest degradation. In contrast, the degradation of the MSFCs could be slowed down and decreased with the increase of MNPs concentration, among which the MSFC250 protein concentration was less than 0.01 µg/µL. The experimental group containing the protease also showed the same change trend (Fig. S5B). To reveal the possible mechanism of MNPs inhibiting SFC degradation, a fluorescence spectroscopy test was performed. As shown in Fig. 5A–B, it could be found that after adding different concentrations of MNPs into the protease XIV solution (Abbreviated as MPP, the following codes correspond to the codes after MSFCs), the peak around 305 nm showed a gradually

decreasing trend. The curves of sample MPP100, MPP150, and MPP250 were flat with the horizontal axis, which might be due to the supersaturation of MNPs complexed with tyrosine and weakened the fluorescence signal. However, when PSC interacted with protease (Abbreviated as PCP, the following codes correspond to the codes after MSFCs), there was no fluorescence signal, which showed that iron atom in MNPs did influence the degradation rate by cross-linking with tyrosine residues. To further prove that iron atom complexed with tyrosine could reduce enzyme activity to inhibit degradation, the protease activity was tested. As shown in Fig. 5C–D, it could be seen that the addition of MNPs slightly reduced protease activity at each period and showed a significant difference. However, the effect of MNPs on protease activity did not show concentration dependent. To exclude the interference of PSC, PSC was co-incubated with protease as the control. The results showed that the effect of PSC on protease activity did not show a significant difference, indicating that iron atoms in MNPs complexed with tyrosine reduced the protease activity.

3.6. MNPs releasing and macrophage phagocytosis analysis

The MNPs were mainly bound to SFC by non-covalent bonds, which led to their weak binding and easy to release MNPs in an aqueous environment. As shown in Fig. 6A, it was found that the release of MNPs of the MSFCs immersed in H$_2$O was significantly higher than that of the PBS and DMEM phase, especially the MSFC250 sample reached a releasing rate of more than 80% after 120 h. Interestingly, the MSFCs immersed in PBS maintained a relatively large releasing of MNPs at 24 h, and then it stabilized except for the MSFC150 sample. After 120 h, the MSFC250 sample with the largest releasing of MNPs only lost about 60%, while the MSFC100 sample kept the smallest releasing of MNPs, only 11%. For the DMEM phase, the releasing of MNPs was generally between the H$_2$O and PBS phases. It should also be noticed that the MSFC50 sample with the highest MNPs content maintained the highest
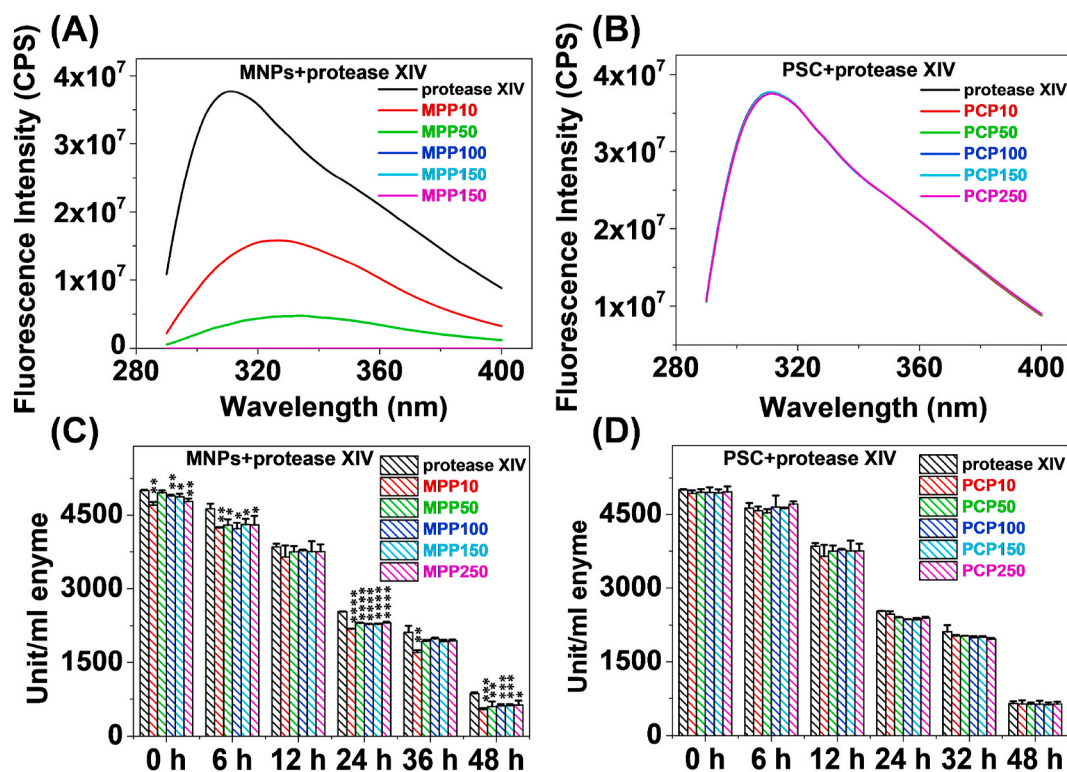

Fig. 5. (A) Fluorescence spectroscopy of MNPs with protease XIV (Abbreviated as MPP, the following codes correspond to the codes after MSFCs), the curves of MPP100, MPP150, and MPP250 were flat with the abscissa axis and were not displayed; (B) Fluorescence spectroscopy of PSC with protease XIV (Abbreviated as PCP, the following codes correspond to the codes after MSFCs), the curves of all the samples almost overlapped and showed a curve; Histogram of protease activity test with MNPs, n = 3 (C) and PSC, n = 3 (D) at 0 h, 4 h, 12 h, 24 h, 32 h and 48 h *P < 0.05, **P < 0.01, ***P < 0.001, ****P < 0.0001 by one-way ANOVA test.
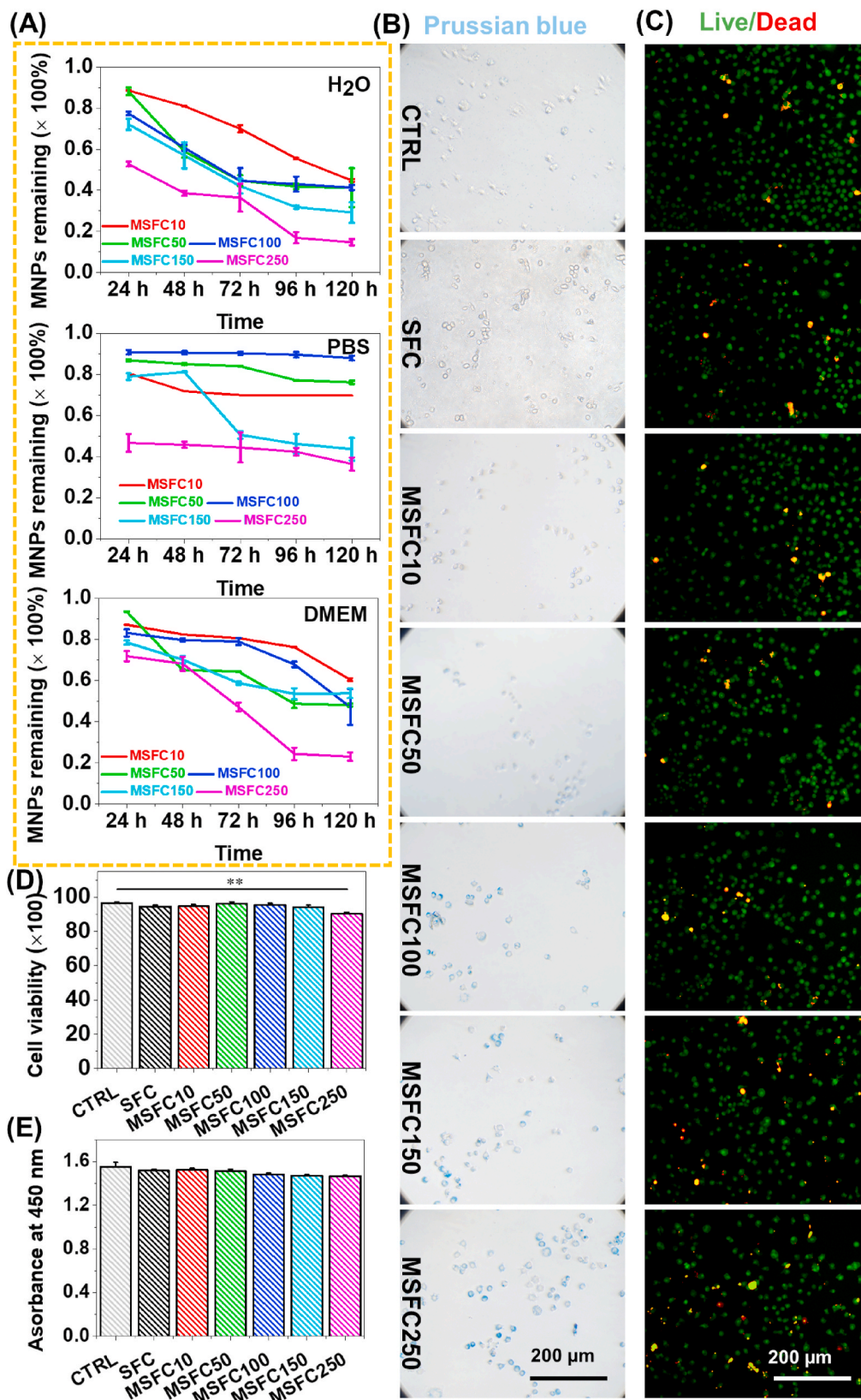
Fig. 6. (A) The MNPs remaining curves of MSFCs at different time points (24, 48, 72, 96, 120 h) in H₂O, PBS and DMEM solution, n = 3; (B) Prussian blue stained images after co-cultivation with RAW264.7 for 36 h in the presence of SFC and MSFCs; Fluorescence microscopy images (C) and statistics (D) showing the staining of live (green)/dead (red) after 36 h cell culture in the presence of SFC and MSFCs, n = 3; (E)The CCK-8 assay results of RAW264.7 on SFC and MSFCs, n = 3. **P < 0.01 by one-way ANOVA test.

releasing rate in the three liquid phases, indicating that MNPs were oversaturated in the scaffold and were easier released in the liquid environment. The released MNPs were dispersed into the surrounding tissues and were easily phagocytized by macrophages. Therefore, the scaffold containing MNPs was immersed into a suspension of macrophages for *in vitro* verification by Prussian blue staining. The results showed that MNPs were indeed easily phagocytized by macrophages and exhibited a gradient accumulation effect (Fig. 6B). Whether the phagocytosed MNPs has a negative effect on macrophages was also evaluated. By staining with phalloidin-FITC (Fig. S6A), it could be found that the cells in the control group and the scaffold group showed strong peripheral F-actin staining, and the microfilaments were well organized, forming a dense network distributed around the cell nucleus. The corresponding quantitative F-actin fluorescence intensity was diagrammed in Fig. S6B, which demonstrated that lower levels of MNPs (MSFC10, MSFC50, MSFC100) phagocytosed by macrophages would not affect the difference in F-actin expression, but higher levels of MNPs (MSFC150, MSFC250) might slightly affect F-actin expression. To further analyze the influence of MNPs on the phagocytosis of macrophages, the cell viability of different sample groups was observed by staining with live/dead cell kit. As shown in Fig. 6C–D, it could be seen that with the increase of the cumulative effect of phagocytized MNPs, the cell viability presented a slight gradient decline. However, only the group of MSFC250 samples showed a significant difference, indicating that the high content of MNPs phagocytized by macrophages might cause excessive apoptosis [42]. We also noticed that macrophage cytokine expression change was critical to vascular remodeling, so its cytokine expression level had also been investigated through ELISA experiments (Fig. 7A). The expression of angiogenic cytokines VEGF did not show regular changes, but MSFC50, MSFC150, and MSFC250 group showed down-regulation, and the expression of the same type of cytokine TGF-β showed an upward trend and only began to decline in MSFC250. The expression of pro-inflammatory cytokines IL-1β and TNF-α showed a slight upward trend overall, and the expression of IL-1β only slightly decreased in the MSFC50 group. Although the phagocytized MNPs would affect the slight expression changes of macrophage cytokines, there was no significant difference from the control group, indicating that the phagocytosis of quantitative MNPs by macrophages would not significantly affect the cytokine expression. However, it was apparent that a reasonable amount of MNPs would also promote the upregulation of some cytokines, especially cytokines that were more conducive to repairing blood vessels. Finally, we also evaluated whether the engulfed MNPs would affect the viability of macrophages by CCK-8 (Fig. 6E). The results showed that the OD values of different scaffold groups were not significantly different from the control group, indicating that the engulfed MNPs would not affect the viability of macrophages. Taken above together, the released MNPs would be phagocytized by macrophages, and would not affect the function of macrophages.

3.7. Cytotoxicity and hemolysis analysis

The HUASMCs were incubated with all scaffolds for 1 d, 2 d, 3 d, and a blank control group was set. As shown in Fig. S7, it could be seen that in the first two days of all experimental groups, cell proliferation and morphology would be significantly affected due to the influence of the new microenvironment provided by the scaffold. However, they did not show obvious MNPs concentration dependence. As time goes by, as the cells gradually adapt to the new microenvironment and become stable, the differences in proliferation and morphology between the experimental and control groups were significantly reduced, and only MSFC250 had a greater impact on the proliferation. In general, MSFCs still have good biocompatibility during a long application cycle *in vivo*, and their cytotoxicity is negligible, so they have promising potential in biomedical applications *in vivo* [43]. To further demonstrate the effect of scaffolds on cell morphology, the HUASMCs cytoskeleton system was observed by immunofluorescence staining (F-actin filaments were stained with phalloidin-FITC) in Fig. 7B. It could be seen that the cells were oval-shaped, not fully stretched in the first 2 days, and the distribution of microfilaments was not obvious. After 3 days, the distribution of HUASMCs microfilaments in the blank control group could be seen, and the clustered cells made the microfilaments spread. A similar microfilaments arrangement could also be seen in the scaffold group, which indicated that the MSFCs had little effect on the HUASMCs cytoskeleton system [44].

Moreover, the HUASMCs' viability was also used to evaluate the safety and potential biomedical value of the material by the CCK-8 experiment. As shown in Fig. 7C, the HUASMCs viability cultured in either of the MSFCs was no significant difference from that in the blank control. It was revealed that the MSFCs had no obvious cytotoxicity. The three experiments showed that the MSFCs had excellent cell compatibility and satisfied the application requirements *in vivo*.

The hemolysis rate was measured by taking blood from the rabbit heart. The representative image was shown in Fig. 7D. The hemolysis rate data of all samples were presented in Fig. 7E. Normally, positive control was considered a 100% hemolytic rate, while negative control was considered a 0% hemolytic rate. The extent of hemolysis rate for different scaffolds of SFC, MSFC10, MSFC50, MSFC100, MSFC150, MSFC250 was found to be 0.18%, 1.74%, 3.74%, 4.83%, 8.74%, 9.67%, respectively. It could be seen that both MSFC150 and MSFC250 had a hemolysis rate of more than 5%, which were not suitable as scaffolds ideal for medical applications. However, the other remaining samples (SFC, MSFC10, MSFC50, MSFC100) showed excellent blood compatibility.

3.8. H&E, immunofluorescence and immunohistochemistry analysis

In vivo biocompatibility of the MSFCs was evaluated in a rabbit subcutaneous transplant model at 1 W, 2 W, 4 W, 16 W. The vital signs of all rabbits implanted scaffolds were intact. No post-operative severe wound complications occurred. The implanted scaffolds were taken out at a predetermined time and observed histologically by H&E staining. As shown in Figs. S8A and a large number of acute inflammatory cells appeared in the scaffolds at 1 W and showed aggregated sheets. At 4W and 8 W, the distribution of inflammatory cells was still more, but it was reduced compared to the first week. It could be observed that the inflammatory cells were significantly reduced after 16 W of implantation, while the scaffolds showed a large area of degradation. To further observe the type of inflammatory cells, the immunofluorescence experiment of the implanted scaffolds was performed. CD14 was an effective cell marker that could be used to detect monocytes and macrophages cells at the inflammation site. The obtained tissue sections were stained by polyclonal anti-CD14, then visualized using Cy3 as a fluorescent developer through antigen-antibody reaction. A small number of monocytes and macrophages appeared in all three scaffolds after 1 W implantation, and then the number increased with time (Fig. S8B). The largest number of monocytes and macrophages stained by CD14 was distributed around scaffolds after 4 W implantation. Meanwhile, monocytes and macrophages after 16 W implantation exhibited a significant reduction in the sections. The result was consistent with the observation of H&E staining. It was consistent with the general rule of physiological function to deal with foreign bodies *in vivo*, indicating that the MSFCs still had good biocompatibility even if magnetic nanoparticles are introduced.

Immunohistochemistry was used to analyze the proliferation of vascular endothelial cells (VECs) on the scaffold. CD34 was a VEC specific surface receptor and highly expressed in VECs. As shown in Fig. 8A–B and S9, the largest VECs were stained by CD34 after 2 W implantation. After 4 W, the number of VECs showed a decreasing trend, which was due to the influence of the most severe inflammatory response. After 16 W, we were surprised to find that VECs had tended to proliferate again and exceeded the number of the second week. The main reason was that the disappearance of inflammation at this stage
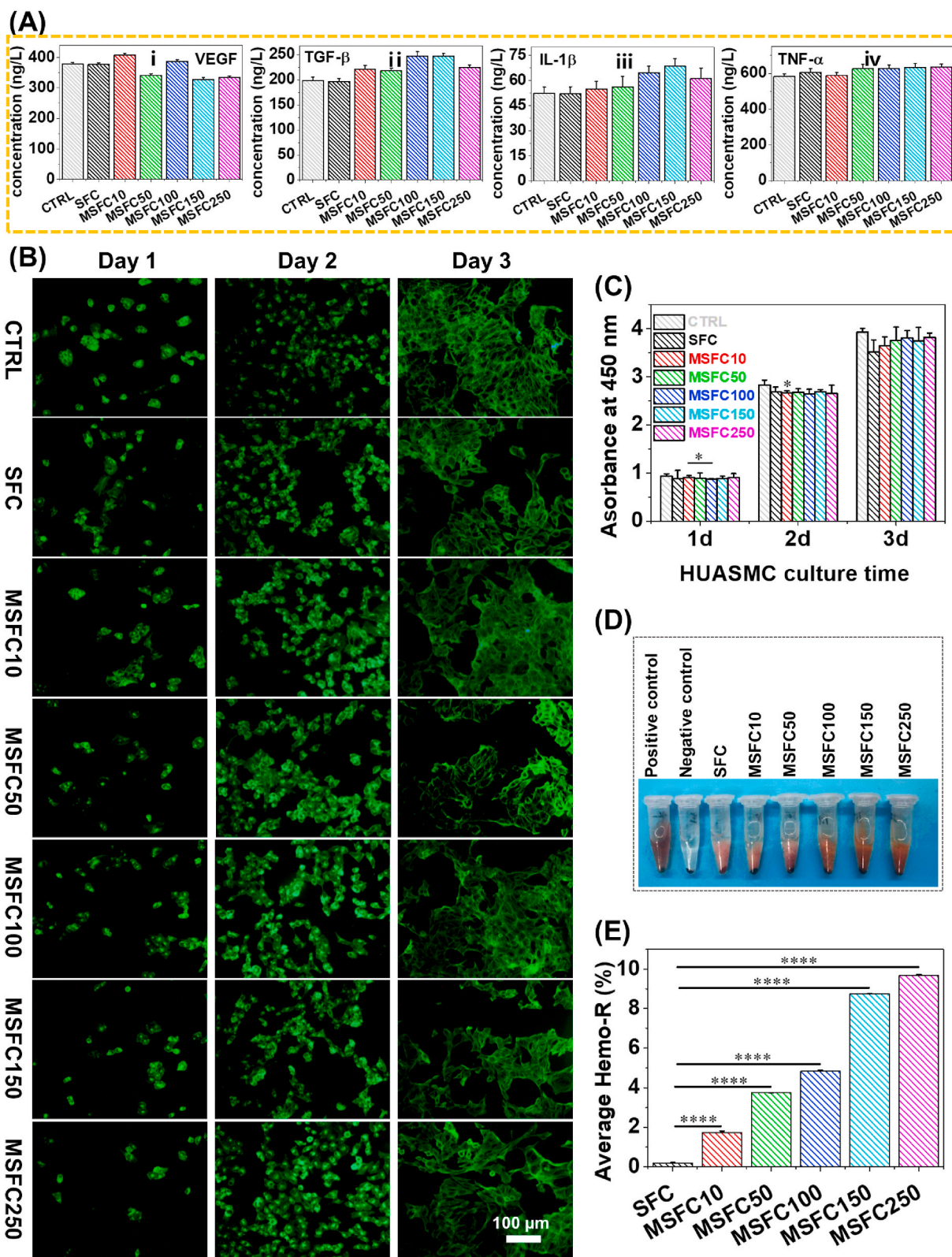
Fig. 7. (A) Cytokines (VEGF, TGF-β,IL-1β and TNF-α) expression assay of RAW264.7 after 36 h cell culture in the presence of SFC and MSFCs, n = 3; (B) The fluorescence microscopy images showing the cytoskeleton system of HUASMCs grown after 1, 2, 3 d cell culture in a blank control, SFC and MSFCs; (C) The CCK-8 assay results of HUASMCs on SFC and MSFCs, n = 3; (D) Representative images of hemolysis test. (E) Statistical results of the hemolysis test, n = 3. *P < 0.05, ****P < 0.0001 by one-way ANOVA test.
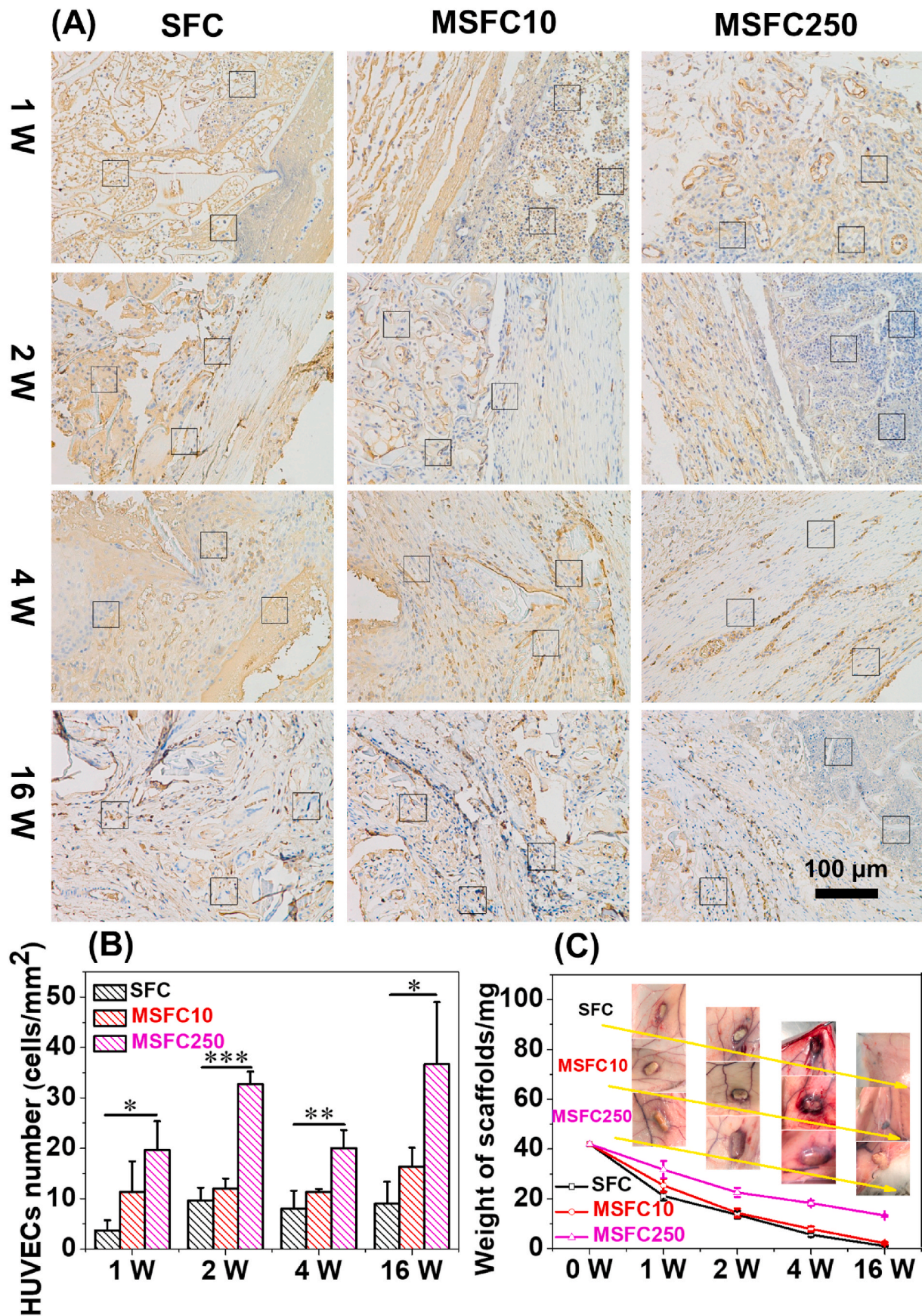
Fig. 8. Immunohistochemistry stained (A) and statistics (B) in different scaffolds (SFC, MSFC10 and MSFC250) with CD34 antibody after 1 W, 2 W, 4 W and 16 W implantation, n = 3; (C) *In vivo* degradation of different scaffolds (SFC, MSFC10 and MSFC250), representative pictures corresponding to each time point were presented. *P < 0.05, **P < 0.01, ***P < 0.001 by one-way ANOVA test.

promoted the activation and proliferation of VECs. Moreover, it was also found that the number of VECs labeled with CD34 on the MSFCs (MSFC10, MSFC250) was significantly higher than that of SFC (as control) at any time.

3.9. In vivo degradation analysis

In vivo degradation of MSFCs was also studied, as shown in Figs. 8C and S10A. After subcutaneous implantation in rabbits, each scaffold was gradually degraded as time goes on. However, it could also be observed that the degradation rate of MSFCs (MSFC10, MSFC250) was significantly slower than that of the SFC group and was correlated with the concentration of MNPs. These results were consistent with *in vitro* degradation, revealing that MNPs could effectively delay SFC degradation. Besides, the scaffold removed from the back of the rabbit needed to be digested by collagenase I and trypsin. To eliminate the influence of the two enzymes on the scaffold, the moist pure SFC was placed in the two enzymes for 24 h in a shaker with 50 rpm/min (Figs. S10B–D). The results showed that the quality of pure SFC after collagenase I and pancreatin treatment did not change significantly compared to before treatment, indicating that the short-term enzymatic digestion treatment would not affect SFC degradation.

4. Discussion

The clinical treatment for LDVJ was a massive challenge. The repair period could reach at least 6 months [45].The long repair period would cause many unknown adverse effects, such as the formation of scars, pathological fibrosis, and suffering for a long time [46,47].

In this study, the developed MSFCs was of higher porosity, which was sufficient to provide an opportunity for nutrient transportation and cell ingrowth (Fig. 1G). Although the MNPs loaded in the SFC occupied space and might lead to smaller pores, the high specific surface area of MNPs would absorb more replacement fluid and increase porosity [48, 49]. The transport of nutrients, the excretion of metabolic wastes, and the exchange of body fluids were all related to the scaffolds' hydrophilic. The research results showed that SFC had the good solution absorption capacity in ddH$_2$O, PBS, and DMEM (Fig. 4E). Furthermore, the MSFCs had both hydrophilic and hydrophobic regions, which means that the scaffold would allow substance exchange and could not compress the tissues by excessive expansion when the scaffold was transplanted into the body [50,51].This was reflected in the swelling rate testing.

The MSFCs as-prepared exhibited the characteristics of delaying degradation and can be regulated (Fig. 4A–B), which was consistent with the result *in vivo* (Figs. 8C and S10A). It is reported that Fe^{3+} could induce a conformational transition of silk fibroin from α-helix or random coil to β-sheet. The main reason was that iron ions might interact with the tyrosine in the tyrosine-rich fragment of SF and formed an intermolecular or intramolecular "Tyr-Fe-Tyr bridge". This "bridge" might reduce the distance between molecular chains, leading to more β-sheets formation within the scaffold [52]. The MNPs used in this study were covered with a network of PSC, which made the obtained MNPs had good dispersion and stability due to steric hindrance. More importantly, the PSC on the surface of MNPs contained many hydroxyl and carboxyl groups, which can bind to the amorphous region of silk fibroin via amide hydrogen bonds. Besides, the network structure of PSC might also make the internal iron atoms bind to the active protease center, possibly forming a "Try-γ-Fe$_2$O$_3$-Try" structure similar to "Tyr-Fe-Tyr," thus reducing the activity of the enzyme and delaying the degradation. The results of FTIR analysis could verify this. Meanwhile, fluorescence spectrum was used to detect the activity of the proteolytic enzyme. The results showed that the pure protease XIV solution showed an obvious absorption peak of tyrosine at 305 nm [53]. The introduction of MNPs significantly weakened the absorption peak, which indicated that the iron atom had complexation with tyrosine in protease XIV (Fig. 5A). In contrast, the direct mixing of PSC with MNPs did not reduce tyrosine

fluorescence absorption (Fig. 5B). BCA was also used to detect the protein concentration of the degradation solution to verify the consistency of the results (Fig. S5). Although the introduction of MNPs could decrease the activity of protease XIV through the complexation of iron atoms on the core surface of MNPs with tyrosine (one of the active sites of protease carboxylic acid side chain) in hydrolase [54], there was no significant content correlation, which might be because of the supersaturation of iron atoms (Fig. 5C–D). XRD, XPS, and NMR have also been performed to explore the chemical reactions and conformational changes to study the effect of MNPs on the degradation delay of MSFCs. The XRD results showed that the addition of MNPs promoted the transition from amorphous peaks to crystalline peaks, and XPS also reflected the same trend (Fig. 2D and S2C-D). The NMR results further confirmed that the above chemical action was hydrogen bond formation (Fig. S3). In summary, the delayed degradation of MSFCs resulted from the synergistic effect of the newly formed hydrogen bonds and the inhibition of hydrolase activity. The schematic diagram of the degradation delay mechanism was also shown in Fig. 9. For Bombyx mori silk, the degradation started from the 11 hydrophilic amorphous segments in the silk heavy chain, such as the C-terminus and N-terminus and the silk light chain, which were composed of completely non-repetitive amino acid sequences [5,54,55]. Then, more crystalline sequences were degraded, and the tightly packed crystalline domains were finally degraded [56]. Therefore, the structure of the primary sequence (amorphous segments: random coil or α-helix) significantly affected the degradation of silk. More importantly, the silk fibroin sequence alignment showed that it was sensitive to various proteases, such as protease XIV, α-chymotrypsin, proteinase K, papain, matrix metalloproteinase, collagenase, etc. [54,55]. Although these proteases were not entirely based on the primary sequence of silk fibroin to regulate the degradation of silk fibroin, the action of an enzyme was often significantly related to its activity. For example, chymotrypsin had 434 cleavage sites in the heavy chain of silk and 81 in the light chain, while protease XIV had 348 cleavage sites in the heavy chain and 41 in the light chain. However, treatment with chymotrypsin with more cleavage sites for 20 days had no quantitative effect on silk fibroin, while protease XIV significantly degraded silk fibroin *in vitro* [55]. Papain was a cysteine protease that mimicked the activity of lysosomal enzymes. It had 26 cleavage sites (amorphous regions) in the heavy chain of silk and 15 cleavage sites in the light chain, which could be significantly degraded silk fibroin within 20 days, but the rate was slower than protease XIV [55]. Based on published research foundation, we believed that it was a good idea to control degradation from the influence of silk fibroin primary sequence structure (amorphous regions) and silk fibroin microenvironment. Our research was based on this idea and believed it was suitable for most protein-based degradable natural materials. Besides, we also believed that the obtained MNPs could improve the degradability of protein scaffolds and apply to other non-protein degradable polymer scaffolds (such as polylactic acid, ʟ-polylactic acid, polyglycolic acid, polyesters, polycarbonates, and hydroxyapatite) [11,57]. The exposed chemical groups of the polymer scaffold (such as –COOH, –OH, –NH$_2$, –CHO) could be non-covalently or covalently bonded to MNPs, or the hydrolase that invades the scaffold can be complexed with iron atoms, synergistically mechanisms that regulate degradation were widely used. There were also many significant universal advantages in application. It was reported that nano-modification of materials could inhibit the harmful invasion of immune cells to the injured site [58,59], and the materials we prepared were also a way of nano-modification. For some drug-carrying materials, delaying degradation could effectively prolong the circulation time in the body to achieve better-targeted drug release effects. Recent studies also pointed out that the scaffolds could be heated by magnetic nanoparticles (MNPs) under an alternating magnetic field (AMF), which dramatically accelerated scaffold degradation [60]. This result used the magnetocaloric effect of MNPs to produce the opposite effect to this article, which showed that the multifunctional effect of MNPs could flexibly regulate the degradation of the scaffold according
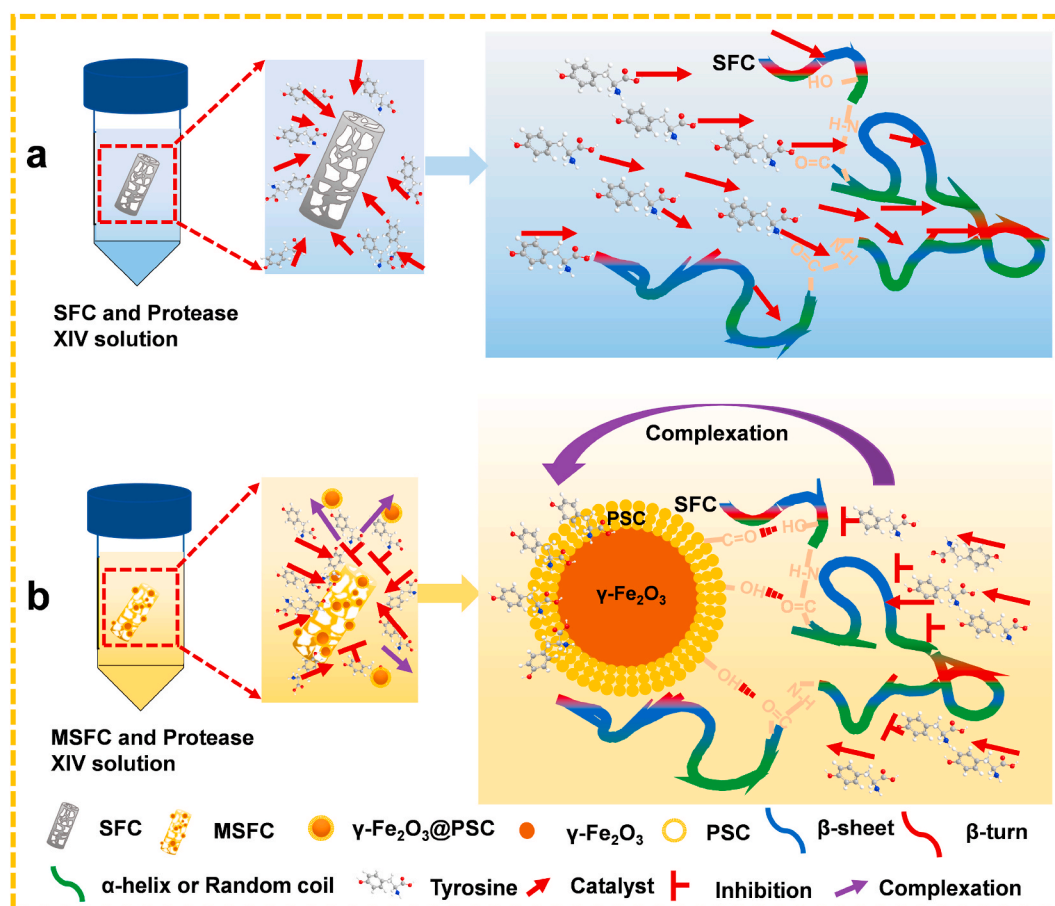
Fig. 9. SFC's degradation mechanism: Tyrosine binding SFC and the hydrogen bonding interaction between SFC and MNPs/iron atoms competes for the active site of the protease (tyrosine) so that the two cooperate to delay the degradation of SFC. Detailed description: Fig. 9a: SFC is immersed in the protease XIV solution, the hydrolase will attack the chemical bond of the scaffold and cause rapid degradation. Fig. 9b: MSFCs is immersed in the protease XIV solution, the hydroxyl and carboxyl groups in MNPs can be combined with the amorphous region of SFC through amide hydrogen bonds. More importantly, the network structure of PSC also makes the internal iron atoms bind to the active center (tyrosine) of the hydrolase, thereby competitively reducing the attack on SFC.

to the application requirements, which might have great instructive significance for the construction of multifunctional implantable scaffold in the future.

The mechanical strength was correlated with the degradation of vascular scaffolds. Especially in the later repair stage, the degradation of the scaffold would significantly weaken the mechanical strength [61]. The deconvolution analysis of the peak of the amide I region showed that MNPs did improve the crystallinity of SFC with the increase of gradient, and MSFC50 showed the greatest mechanical strength. We believed that the strength of the scaffolds was related to the 3-dimensional structure and internal crystalline structure of the scaffolds, which was consistent with the results of the pore size and porosity of MSFC50. Besides, according to the principle of dispersion strengthening, the reasonable distribution of an appropriate number of particles in another phase could greatly enhance the mechanical strength, which we believed was also one reason.

The MNPs were loaded on SFC with non-covalent bonds and were easily released from the scaffold. Interestingly, MSFCs immersed in H_2O showed more release than that in PBS and DMEM. We think it was mainly related to the pH environment in the liquid phase where MSFCs were located. The pH of the H_2O we used was 6.0–7.0, which was weakly acidic compared to the pH of PBS and DMEM. The weakly acidic liquid environment weakened the hydrogen bonding between MNPs and SFC, replacing a part of the hydrogen ions, resulting in more MNPs being released. The release of MNPs in DMEM was more than that in PBS, which might be because the chemical groups exposed by glucose, glutamine, and sodium pyruvate in DMEM would slightly replace a part

of the hydrogen ions, resulting in more release than PBS [62,63]. The released MNPs were also easily phagocytized by macrophages. Macrophages were important regulatory cells for vascular remodeling and could secrete various regulatory factors to promote vascular repair. In recent years, many studies had shown that MNPs could regulate the appearance of macrophages, such as the transition to M2 type that was more conducive to vascular repair, even if this regulation were strictly content dependent. Our research results showed that MNPs maintained a higher release rate in H_2O and showed the best stability in PBS (Fig. 6A). However, our research sample was under the shaker with 180 rpm/min, and the actual *in vivo* environment was gentler than *in vitro*, so we believed that the release rate *in vivo* was much lower than *in vitro*. More importantly, the F-actin expression of macrophages cultured on the MSFCs showed a dose-dependent manner, and a lower content of MNPs was phagocytosed without destroying the F-actin cytoskeleton network, which also provided a reference for the amount of MNPs added in subsequent *in vivo* applications (Fig. S6). The subsequent live/dead cell staining also showed consistent results (Fig. 6C–D). The overall results of cytokine expression showed that MNPs might cause the up-regulation of macrophage cytokines, but the MSFC250 group was mainly down-regulated, which indicated that the content of MNPs in the MSFC250 group alone was not conducive to the function of macrophages (Fig. 7A). The CCK-8 results also showed consistent results (Fig. 6E).

Good biological safety was one of the essential requirements for the application of vascular scaffolds in the body. HUASMC was an important cell for vascular remodeling, maintaining vascular structure, mechanical

properties, and regulating vasoconstriction and relaxation [64]. The HUASMC could preferentially reshape the structure and skeleton of blood vessels when LDVJ occurred. Our *in vitro* results show that the cells grow well on all materials, the skeletal shape is complete, and the cell viability value is above 90% (Fig. S7 and 7B-C). The hemolysis test also proved that the composite scaffolds had reached the national standard for interventional medical devices below 5% except for MSFC150 and MSFC250 (Fig. 7D and E) [65]. The rabbit subcutaneous transplantation experiment also evaluated the safety and function *in vivo*. H&E staining showed slightly more inflammatory cells in MSFCs than in the SFC group (as control) at 2 W and 8 W (Fig. S8A). This might be because a minimal amount of Fe^{3+} was released under acidic enzymes in the body, causing some inflammation induced by the oxidative stress response. However, this effect was minimal, and the difference was not significant, which could be observed at 16 W. The results of CD14-labeled monocytes and macrophages were consistent with H&E (Fig. S8B). The inflammatory response reached the maximum at 8 W, and it was significantly reduced after 16 W, which was also in line with the general law of the allogeneic antigen effect. More interestingly, the rapid proliferation of VECs was crucial as a key step in vascular endothelial revascularization [66]. Our results showed that the expression level of VECs on MSFCs was always higher than that of SFC at each time point, which also proved that MNPs might induce VECs to migrate around the scaffold or regulate the microenvironment around the scaffold (for example, in response to macrophage migration to promote the high expression of growth factors, etc.), thereby promoting the proliferation of VEC. This also showed that MSFCs had great application potential for repairing LDVJ in the future (Fig. 8A–B and S9).

Finally, the introduction of MNPs could play more roles in repairing LDVJ, including as a control-release carrier of anticoagulants and magnetic resonance imaging (MRI) agent. Thrombosis caused by platelet aggregation was one of the major challenges in repairing vascular injury. If the anticoagulant drugs (such as rapamycin, aspirin, and heparin sodium) were loaded to MNPs, and the half-life was maintained long enough, an excellent repair effect will be achieved. Furthermore, the MNPs were outstanding magnetic resonance contrast agents, which could participate in real-time observation of the repair progress of blood vessels and the patency of blood flow to implement an early intervention.

5. Conclusion

A composite silk fibroin-based scaffold loaded with MNPs has been developed. Compared with traditional SFC, MSFCs has delayed degradation rate which might be because of the synergistic effect of the newly formed hydrogen bonds and the inhibition of hydrolase activity. The formation of hydrogen bonds between MNPs and SFC strengthened the structure of the scaffold. And the complexation of iron atoms and tyrosine decreased the activity of hydrolase. The presentation of MNPs would not affect the biocompatibility of MSFCs, especially the macrophage function. And it would promote the proliferation of VECs. The MSFCs as prepared would be used as one of the effective candidate scaffolds for the repair of LDVJ.

CRediT authorship contribution statement

Xin Liu: Conceptualization, Methodology, Formal analysis, Investigation, Writing – original draft. **Yuxiang Sun:** Methodology, Formal analysis, Writing – review & editing. **Bo Chen:** Formal analysis. **Yan Li:** Formal analysis, Writing & Revising, Supervision. **Peng Zhu:** Conceptualization. **Peng Wang:** Conceptualization, Methodology. **Sen Yan:** Writing – review & editing. **Yao Li:** Writing – review & editing. **Fang Yang:** Supervision, Formal analysis. **Ning Gu:** Supervision, Supervision.

Declaration of competing interest

The authors declare that they have no known competing financial interests or personal relationships that could have appeared to influence the work reported in this paper.

Appendix A. Supplementary data

Supplementary data to this article can be found online at https://doi.org/10.1016/j.bioactmat.2021.04.036.

References

[1] K. Banno, M.C. Yoder, Tissue regeneration using endothelial colony-forming cells: promising cells for vascular repair, Pediatr. Res. 83 (2018) 283–290.

[2] V. Makaloski, A. Stellmes, D. Wyss, S. Weiss, D. Becker, T.R. Wyss, J. Schmidli, Posterior approach for revascularization in blunt popliteal vessel injury, Ann. Vasc. Surg. 48 (2018) 89–96.

[3] M. Liang, J.J. Rong, J.Y. Sun, X.Z. Wang, F. Li, G. Wang, Y.C. Liang, Y.L. Han, Feasibility study of emergency intervention for vascular injury outside the hospital, Mil. Med. Res. 3 (2016) 36.

[4] X. Liu, B. Chen, Y. Li, Y. Kong, M. Gao, L.Z. Zhang, N. Gu, Development of an electrospun polycaprolactone/silk scaffold for potential vascular tissue engineering applications, J. Bioact. Compat Polym. 36 (2020) 59–76.

[5] K. Numata, P. Cebe, D.L. Kaplan, Mechanism of enzymatic degradation of beta-sheet crystals, Biomaterials 31 (2010) 2926–2933.

[6] Y. Chen, M. Shafiq, M. Liu, Y. Morsi, X. Mo, Advanced fabrication for electrospun three-dimensional nanofiber aerogels and scaffolds, Bioact. Mater. 5 (2020) 963–979.

[7] A. Kjar, B. McFarland, K. Mecham, N. Harward, Y. Huang, Engineering of tissue constructs using coaxial bioprinting, Bioact. Mater. 6 (2021) 460–471.

[8] H.Y. Yuan, C.Y. Chen, Y.H. Liu, T. Lu, Z.S. Wu, Strategies in cell-free tissue-engineered vascular grafts, J. Biomed. Mater. Res., Part A 108 (2020) 426–445.

[9] A. Mahara, K.L. Kiick, T. Yamaoka, In vivo guided vascular regeneration with a non-porous elastin-like polypeptide hydrogel tubular scaffold, J. Biomed. Mater. Res., Part A 105 (2017) 1746–1755.

[10] J.J. Chi, X.X. Zhang, C.W. Chen, C.M. Shao, Y.J. Zhao, Y.G. Wang, Antibacterial and angiogenic chitosan microneedle array patch for promoting wound healing, Bioact. Mater. 5 (2020) 253–259.

[11] M.P. Nikolova, M.S. Chavali, Recent advances in biomaterials for 3D scaffolds: a review, Bioact. Mater. 4 (2019) 271–292.

[12] X.R. Xie, Y.J. Chen, X.Y. Wang, X.Q. Xu, Y.H. Shen, A.U.R. Khan, A. Aldalbahi, A.E. Fetz, G.L. Bowlin, M. El-Newehy, X.M. Mo, Electrospinning nanofiber scaffolds for soft and hard tissue regeneration, J. Mar. Sci. Technol. 59 (2020) 243–261.

[13] S. Tandon, B. Kandasubramanian, S.M. Ibrahim, Silk-based composite scaffolds for tissue engineering applications, Ind. Eng. Chem. Res. 59 (2020) 17593–17611.

[14] E.C. Filipe, M. Santos, J. Hung, B.S.L. Lee, N. Yang, A.H.P. Chan, M.K.C. Ng, J. Rnjak-Kovacina, S.G. Wise, Rapid endothelialization of off-the-shelf small diameter silk vascular grafts, JACC: Basic to Translational Science 3 (2018) 38–53.

[15] Y. Yao, A.M. Zaw, D.E.J. Anderson, M.T. Hinds, E.K.F. Yim, Fucoidan functionalization on poly(vinyl alcohol) hydrogels for improved endothelialization and hemocompatibility, Biomaterials 249 (2020) 120011.

[16] C. Baley, M. Gomina, J. Breard, M. Bourmaud, P. Davies, Variability of mechanical properties of flax fibres for composite reinforcement. A review, Ind. Crop. Prod. 145 (2020) 111984.

[17] S.S. Panchal, D.V. Vasava, Biodegradable polymeric materials: synthetic approach, ACS Omega 5 (2020) 4370–4379.

[18] D.R. Griffin, M.M. Archang, C.-H. Kuan, W.M. Weaver, J.S. Weinstein, A.C. Feng, A. Ruccia, E. Sideris, V. Ragkousis, J. Koh, M.V. Plikus, D. Di Carlo, T. Segura, P.O. Scumpia, Activating an adaptive immune response from a hydrogel scaffold imparts regenerative wound healing, Nat. Mater. 20 (2020) 560–569.

[19] J. Zhou, Z.Y. Zhao, R.M. Hu, T. Fan, Y.P. Liu, M. Lu, Magnetic silk fabrics through swelling-fixing method with Fe3O4 nanoparticles, Surf. Coating. Technol. 342 (2018) 23–28.

[20] W.T. Jung, J.W. Jeon, H.S. Jang, D.Y. Kim, H.K. Lee, B.H. Kim, Commercial silk-based electronic textiles for NO2 sensing, Sens. Actuators, B 307 (2020) 127596.

[21] R. Konwarh, Can the venerated silk be the next-generation nanobiomaterial for biomedical-device designing, regenerative medicine and drug delivery? Prospects and hitches, Bio-Des. Manuf. 2 (2019) 278–286.

[22] F. Jeffery, C. La Mattina, T. Tuton-Blasingame, Y. Hsia, E. Gnesa, L. Zhao, A. Franz, C. Vierra, Microdissection of black widow spider silk-producing glands, Jove-J Vis. Exp. (2011), e2382.

[23] X. Zhao, Z.Y. Chen, Y.X. Liu, Q. Huang, H.D. Zhang, W. Ji, J.N. Ren, J.S. Li, Y.J. Zhao, Silk fibroin microparticles with hollow mesoporous silica nanocarriers

encapsulation for abdominal wall repair, Adv. Healthcare Mater. 7 (2018) 1801005.

[24] W.W. Huang, S.J. Ling, C.M. Li, F.G. Omenetto, D.L. Kaplan, Silkworm silk-based materials and devices generated using bio-nanotechnology, Chem. Soc. Rev. 47 (2018) 6486–6504.

[25] J.B. Wu, Z.Z. Zheng, G. Li, D.L. Kaplan, X.Q. Wang, Control of silk microsphere formation using polyethylene glycol (PEG), Acta Biomater. 39 (2016) 156–168.

[26] M.M. Fernandes, D.M. Correia, A. da Costa, S. Ribeiro, M. Casal, S. Lanceros-Mendez, R. Machado, Multifunctional magnetically responsive biocomposites based on genetically engineered silk-elastin-like protein, Compos. B Eng. 153 (2018) 413–419.

[27] P. Cebe, B.P. Partlow, D.L. Kaplan, A. Wurm, E. Zhuravlev, C. Schick, Silk I and Silk II studied by fast scanning calorimetry, Acta Biomater. 55 (2017) 323–332.

[28] S. Toghyani, M. Khodaei, M. Razavi, Magnesium scaffolds with two novel biomimetic designs and MgF2 coating for bone tissue engineering, Surf. Coating. Technol. 395 (2020) 125929.

[29] M.S. Manjari, K.P. Aaron, C. Muralidharan, C. Rose, Highly biocompatible novel polyphenol cross-linked collagen scaffold for potential tissue engineering applications, React. Funct. Polym. 153 (2020) 104630.

[30] L.H. Reddy, J.L. Arias, J. Nicolas, P. Couvreur, Magnetic nanoparticles: design and characterization, toxicity and biocompatibility, pharmaceutical and biomedical applications, Nanoscale Adv 112 (2012) 5818–5878.

[31] K. Zhu, Y.M. Ju, J.J. Xu, Z.Y. Yang, S. Gao, Y.L. Hou, Magnetic nanomaterials: chemical design, synthesis, and potential applications, Acc. Chem. Res. 51 (2018) 404–413.

[32] A. El-Fiqi, N. Mandakhbayar, S.B. Jo, J.C. Knowles, J.-H. Lee, H.-W. Kim, Nanotherapeutics for regeneration of degenerated tissue infected by bacteria through the multiple delivery of bioactive ions and growth factor with antibacterial/angiogenic and osteogenic/odontogenic capacity, Bioact. Mater. 6 (2021) 123–136.

[33] H. Perea, J. Aigner, U. Hopfner, E. Wintermantel, Direct magnetic tubular cell seeding: a novel approach for vascular tissue engineering, Cells Tissues Organs 183 (2006) 156–165.

[34] B. Chen, J. Sun, F. Fan, X. Zhang, Z. Qin, P. Wang, Y. Li, X. Zhang, F. Liu, Y. Liu, M. Ji, N. Gu, Ferumoxytol of ultrahigh magnetization produced by hydrocooling and magnetically internal heating co-precipitation, Nanoscale 10 (2018) 7369–7376.

[35] J. Rnjak-Kovacina, L.S. Wray, K.A. Burke, T. Torregrosa, J.M. Golinski, W. Huang, D.L. Kaplan, Lyophilized silk sponges: a versatile biomaterial platform for soft tissue engineering, ACS Biomater. Sci. Eng. 1 (2015) 260–270.

[36] C. Pignatelli, G. Perotto, M. Nardini, R. Cancedda, M. Mastrogiacomo, A. Athanassiou, Electrospun silk fibroin fibers for storage and controlled release of human platelet lysate, Acta Biomater. 73 (2018) 365–376.

[37] D. Ji, Y.-B. Deng, P. Zhou, Folding process of silk fibroin induced by ferric and ferrous ions, J. Mol. Struct. 938 (2009) 305–310.

[38] Y. Song, Z. Lin, L. Kong, Y. Xing, N. Lin, Z. Zhang, B.-H. Chen, X.-Y. Liu, Meso-functionalization of silk fibroin by upconversion fluorescence and near infrared in vivo biosensing, Adv. Funct. Mater. 27 (2017) 1700628.

[39] Z.H. Zhu, S.J. Ling, J.J. Yeo, S.W. Zhao, L. Tozzi, M.J. Buehler, F. Omenetto, C. M. Li, D.L. Kaplan, High-strength, durable all-silk fibroin hydrogels with versatile processability toward multifunctional applications, Adv. Funct. Mater. 28 (2018) 1704757.

[40] G. Wu, H. Deng, T. Jiang, H. Tu, J. Chen, Y. Zhan, Y. Wang, X. Ma, Regulating the gaps between folds on the surface of silk fibroin membranes via LBL deposition for improving their biomedical properties, Colloids Surf., B 154 (2017) 228–238.

[41] C.Y. Jiang, X.Y. Wang, R. Gunawidjaja, Y.H. Lin, M.K. Gupta, D.L. Kaplan, R. R. Naik, V.V. Tsukruk, Mechanical properties of robust ultrathin silk fibroin films, Adv. Funct. Mater. 17 (2007) 2229–2237.

[42] S.K. Samal, M. Dash, T. Shelyakova, H.A. Declercq, M. Uhlarz, M. Banobre-Lopez, P. Dubruel, M. Cornelissen, T. Herrmannsdorfer, J. Rivas, G. Padeletti, S. De Smedt, K. Braeckmans, D.L. Kaplan, V.A. Dediu, Biomimetic magnetic silk scaffolds, ACS Appl. Mater. Interfaces 7 (2015) 6282–6292.

[43] J. Wu, J. Zhu, Q. Wu, Y. An, K. Wang, T. Xuan, J. Zhang, W. Song, H. He, L. Song, J. Zheng, J. Xiao, Mussel-inspired surface immobilization of heparin on magnetic nanoparticles for enhanced wound repair via sustained release of a growth factor and M2 macrophage polarization, ACS Appl. Mater. Interfaces 13 (2021) 2230–2244.

[44] E.A. Naumenko, I.D. Guryanov, R. Yendluri, Y.M. Lvov, R.F. Fakhrullin, Clay nanotube-biopolymer composite scaffolds for tissue engineering, Nanoscale 8 (2016) 7257–7271.

[45] Y. Zhuang, C. Zhang, M. Cheng, J. Huang, Q. Liu, G. Yuan, K. Lin, H. Yu, Challenges and strategies for in situ endothelialization and long-term lumen patency of vascular grafts, Bioact. Mater. 6 (2021) 1791–1809.

[46] X. Liu, B. Chen, Y. Li, Y. Kong, M. Gao, L.Z. Zhang, N. Gu, Development of an electrospun polycaprolactone/silk scaffold for potential vascular tissue engineering applications, J. Bioact. Compat Polym. (2020), 0883911520973244.

[47] B. Zhao, Z.H. Zhao, J.X. Ma, X.L. Ma, Repairing peripheral nerve defects with revascularized tissue-engineered nerve based on a vascular endothelial growth factor-heparin sustained release system, J. Tissue Eng. Regener. Med. 14 (2020) 819–828.

[48] S. Singh, D. Dutt, P. Kaur, H. Singh, N.C. Mishra, Microfibrous paper scaffold for tissue engineering application, J. Biomat. Sci-Poly M 31 (2020) 1091–1106.

[49] H.A. Almeida, P.J. Bartolo, Biomimetic boundary-based scaffold design for tissue engineering applications, Methods Mol. Biol. 2147 (2021) 3–18.

[50] G. Selvakumar, L. Suguna, Fabrication and characterization of collagen-oxidized pullulan scaffold for biomedical applications, Int. J. Biol. Macromol. 164 (2020) 1592–1599.

[51] L.Y. Wang, J.R. Li, D. Zhang, S.S. Ma, J.N. Zhang, F. Gao, F.X. Guan, M.H. Yao, Dual-enzymatically crosslinked and injectable hyaluronic acid hydrogels for potential application in tissue engineering, RSC Adv. 10 (2020) 2870–2876.

[52] Q.S. Liu, X. Wang, X.Y. Tan, X.Q. Xie, Y. Li, P. Zhao, Q.Y. Xia, A strategy for improving the mechanical properties of silk fiber by directly injection of ferric ions into silkworm, Mater. Des. 146 (2018) 134–141.

[53] Q. Liu, X. Wang, X. Tan, X. Xie, Y. Li, P. Zhao, Q. Xia, A strategy for improving the mechanical properties of silk fiber by directly injection of ferric ions into silkworm, Mater. Des. 146 (2018) 134–141.

[54] J. Brown, C.L. Lu, J. Coburn, D.L. Kaplan, Impact of silk biomaterial structure on proteolysis, Acta Biomater. 11 (2015) 212–221.

[55] T. Wongpinyochit, B.F. Johnston, F.P. Seib, Degradation behavior of silk nanoparticles-enzyme responsiveness, ACS Biomater. Sci. Eng. 4 (2018) 942–951.

[56] K. Numata, D.L. Kaplan, Mechanisms of enzymatic degradation of amyloid beta microfibrils generating nanofilaments and nanospheres related to cytotoxicity, Biochemistry 49 (2010) 3254–3260.

[57] T. Li, J. Chang, Y.F. Zhu, C.T. Wu, 3D printing of bioinspired biomaterials for tissue regeneration, Adv. Healthcare Mater. 9 (2020) 2000208.

[58] Q.Y. Wang, Y.Q. Tang, Q.F. Ke, W.J. Yin, C.Q. Zhang, Y.P. Guo, J.J. Guan, Magnetic lanthanum-doped hydroxyapatite/chitosan scaffolds with endogenous stem cell-recruiting and immunomodulatory properties for bone regeneration, J. Mater. Chem. B 8 (2020) 5280–5292.

[59] X.P. Wang, S. Ihara, X. Li, A. Ito, Y. Sogo, Y. Watanabe, A. Yamazaki, N.M. Tsuji, T. Ohno, Rod-scale design strategies for immune-targeted delivery system toward cancer immunotherapy, ACS Nano 13 (2019) 7705–7715.

[60] L. Hao, J. Li, P. Wang, Z. Wang, Z. Wu, Y. Wang, Z. Jiao, M. Guo, T. Shi, Q. Wang, Y. Ito, Y. Wei, P. Zhang, Spatiotemporal magnetocaloric microenvironment for guiding the fate of biodegradable polymer implants, Adv. Funct. Mater. (2021) 2009661.

[61] A. Sharma, S. Molla, K.S. Katti, D.R. Katti, Multiscale models of degradation and healing of bone tissue engineering nanocomposite scaffolds, J. Nanomech. Micromech. 7 (2017). UNSP 04017015.

[62] H.C. Zhang, Z.N. Liu, H. Fu, Pillararenes trimer for self-assembly, Nanomaterials 10 (2020) 651.

[63] X.Z. Li, P.J. Hu, Z.D. Zhu, G.X. Zhu, X.P. Shen, M. Wang, Y. Sun, D.X. Feng, Release mechanisms and properties of pH-responsive drug nanocarriers, Chin. J. Inorg. Chem. 34 (2018) 1399–1412.

[64] X.Z. Wan, Y.F. Wang, X.X. Jin, P.F. Li, J. Yuan, J. Shen, Heparinized PCL/keratin mats for vascular tissue engineering scaffold with potential of catalytic nitric oxide generation, J. Biomat. Sci-Polym E 29 (2018) 1785–1798.

[65] L. Yang, X.F. Li, D.M. Wang, S.F. Mu, W.H. Lv, Y.W. Hao, X.S. Lu, G.J. Zhang, W. B. Nan, H.L. Chen, L.Q. Xie, Y.J. Zhang, Y.Z. Dong, Q.Q. Zhang, L. Zhao, Improved mechanical properties by modifying fibrin scaffold with PCL and its biocompatibility evaluation, J. Biomat. Sci-Polym E 31 (2020) 658–678.

[66] J.G. Li, F. Wu, K. Zhang, Z.K. He, D. Zou, X. Luo, Y.H. Fan, P. Yang, A.S. Zhao, N. Huang, Controlling molecular weight of hyaluronic acid conjugated on amine-rich surface: toward better multifunctional biomaterials for cardiovascular implants, ACS Appl. Mater. Interfaces 9 (2017) 30343–30358.